

Article

# Geochemical Characterization of Bauxite Deposits from the Abruzzi Mining District (Italy)

Francesco Putzolu <sup>1,\*</sup> , Armando Piccolo Papa <sup>1</sup>, Nicola Mondillo <sup>1</sup>, Maria Boni <sup>1</sup>,  
Giuseppina Balassone <sup>1</sup>  and Angela Mormone <sup>2</sup>

<sup>1</sup> Dipartimento Scienze della Terra, dell'Ambiente e delle Risorse, Università di Napoli Federico II, Complesso Universitario di Monte Sant'Angelo, Via Cintia, 80126 Napoli, Italy; iccolopapaarmando@hotmail.it (A.P.P.); nicola.mondillo@unina.it (N.M.); maria.boni@unina.it (M.B.); giuseppina.balassone@unina.it (G.B.)

<sup>2</sup> INGV—Osservatorio Vesuviano, Via Diocleziano 328, 80124 Napoli, Italy; angela.mormone@ov.ingv.it

\* Correspondence: francesco.putzolu@unina.it

Received: 30 May 2018; Accepted: 10 July 2018; Published: 12 July 2018



**Abstract:** The Abruzzi bauxite district includes the deposits located on the Campo Felice plateau and those of the Monti d'Ocre, which had been mined in the first part of the 20th century. Bauxite is of the karst type, with textures ranging between oolitic and oolitic-conglomeratic, the latter suggesting a partial reworking of evolved lateritic soils. The high contents of Al<sub>2</sub>O<sub>3</sub> and Fe<sub>2</sub>O<sub>3</sub> (average values 53.76 and 21.76 wt %, respectively) are associated with the presence of boehmite, hematite, and minor goethite. SiO<sub>2</sub> and TiO<sub>2</sub> have average values of 7.79 and 2.75 wt %, corresponding to the presence of kaolinite, anatase and rutile. Among the minor so-called “bauxitophile” elements V, Co, Ni, Cr and Zr, the most enriched is Cr, with an average value of 0.07 wt %. Nickel has an average value of 210.83 ppm. Vanadium shows an average value of 266.57 ppm, whereas the average Co concentration is 35.89 ppm. The total rare earth elements (REE) concentration in the sampled bauxite sites is variable between ca. 700 and 550 ppm. Among REEs, the most abundant element is Ce, with Ce anomalies commonly associated with authigenic REE-fluoro-carbonates, probably produced after the REEs remobilization from primary detrital minerals and their precipitation in neo-formed phases during the bauxitization process. Scandium and Ga occur in small amounts (57 and 60 ppm, respectively), but geochemical proxies of their remobilization and uptake in neo-formed minerals (Fe- and Al-(hydr)oxides, respectively) have been observed. The mean Eu/Eu\* and Al<sub>2</sub>O<sub>3</sub>/TiO<sub>2</sub> ratios and the Ni-Cr contents of the Abruzzi bauxites suggest that the parent rock of these deposits was a material of acid affinity, likely corresponding to volcanic tephra or eolic loess-type sands.

**Keywords:** karst bauxite; rare earth elements; scandium; gallium; Abruzzi; Italy

## 1. Introduction

Bauxites are economic concentrations of aluminum, developed from the weathering of aluminosilicate-rich parent rocks. These residual deposits are mainly formed under humid tropical to sub-tropical climates, with rainfalls in excess of 1.2 m and annual mean temperatures higher than 22 °C [1]. Aluminum in bauxites is known to be precipitated in form of gibbsite [Al(OH)<sub>3</sub>] or amorphous Al-hydroxides. Bauxites that were subjected to several diagenetic stages consist mainly of boehmite [ $\gamma$ -AlO(OH)], which is less hydrated than gibbsite, and diaspore [ $\alpha$ -AlO(OH)]. Iron is separated from aluminum and is frequently concentrated as hematite, goethite, and less as lepidocrocite.

As of January 2016, the worldwide bauxite reserves stood at 27.5 billion tonnes. Global bauxite production was estimated at 279.7 million tonnes in 2015, down 0.3% year-over-year, attributed to a production decline during the year in Brazil, Indonesia and China [2]. In 2017, the world bauxite

resources were estimated to be 55–75 billion tonnes [3], comprising Africa (32%), Oceania (23%), South America and the Caribbean (21%), Asia (18%), and elsewhere (6%).

Though several intense paleoweathering periods have been recorded in the Tethys realm from Upper Paleozoic to Mesozoic, the Cretaceous-Eocene interval is considered the most favorable for bauxitization [4]. In the European continent, Cretaceous marked one distinctive period of closure of part of the Tethys Ocean accompanied by collision, uplift, and exhumation of both ophiolitic suites and sedimentary successions. Many of the circum-Mediterranean bauxites, including those located in the Italian peninsula, are Cretaceous in age, all formed in karstic environments (“karst bauxites”, after [5]) on exhumed carbonate rocks, which behaved as both physical and chemical traps. The karstic network provided optimum drainage, necessary for further desilicification of bauxites, as well as providing a protected environment from later surface erosion [5]. Most European bauxites are characterized by minerals deposited in high Eh conditions, and are rich in “bauxitophile” trace elements, like V, Co, Ni, Cr, Zr and local REEs [5].

Bauxite deposits, at present uneconomic due to their small size and scattered distribution, occur along a Cretaceous stratigraphic gap in the carbonate platforms of Central and Southern Italy (Figure 1) in Abruzzi-Molise, Campania and Apulia regions. In the Abruzzi district bauxite was discovered by J.A. Meissonnier in 1857, and the first Italian mine for aluminum production was opened near the village of Lecce nei Marsi in 1905. Further bauxite outcrops were soon located in the whole Abruzzi region, as well as in nearby Campania [6]. Several bauxite concentrations were then discovered also in Northern (Gargano, Murge) and Southern (Salento) Apulia at the beginning of the 20th century [6].

The main bauxite horizons in Central and Southern Apennines are Aptian to Turonian in age, and prevalingly boehmitic [6–11]. Despite their low economic value, these bauxites can be considered as a model analogue for other, far more economic karst bauxite deposits in the world. The data presented here refer to two old mining areas (Campo Felice and Monti d’Ocre) in the Abruzzi region, where bauxites were exploited in the first part of the 20th century. The present study integrates the mineralogical and petrographic characterization of the Abruzzi bauxite conducted by [7]. The main aim of this research is to describe the distribution and the behavior of the minor and trace elements (with particular attention to the distribution of REEs) during the bauxitization process, and their relationship with the main mineral components of the bauxite deposits. A particular focus will be also devoted to discuss the nature of the parent material of the studied bauxites that, as for other karst bauxites of the world, is not always obvious, and to their comparison with other similar deposits of the Mediterranean realm.

## 2. Geological Setting

Abruzzi karst bauxites are incorporated in a thick Meso-Cenozoic carbonate succession, which is part of Apennine Carbonate Platform (ACP) [12], and occurs within the Apennine fold and thrust belt (Figure 1). This belt forms part of the Africa-verging mountain system in the Alpine-Mediterranean area that evolved within the framework of a convergent motion between the African and European plates since Late Cretaceous [13]. Up to Oligocene, a roughly North-South convergence was dominant in the belt. During Neogene, an east-directed thrusting toward the Apulian continental margin prevailed, as a response to the opening of the Tyrrhenian Sea [14–17]. During this time, the tectono-stratigraphic evolution of the Adria experienced several episodes of coeval uplift and drowning. Different sectors of the Apennine and Apulian platforms were thus characterized by changes in the paleoenvironments, leading to different stratigraphic records (from shallow-water to slope and basin), as well as to the development of bauxite layers. The Albian-Eocene interval was also characterized by the occurrence of anorogenic magmatism and synsedimentary extensional faulting that, along with the variable sedimentary facies distribution, point to a crustal-scale extensional tectonics [18].

The Apennine sedimentary successions consist mainly of carbonates, shales and cherty carbonates (the latter limited to basinal facies), ranging in age between Late Triassic and Early Miocene with substantial facies and thickness variations [19]. The Mesozoic sediments enclose, from the east to the

west, a shallow water carbonate platform-dominated succession (Apulian Platform), deep basinal successions (Umbria-Marche in the Northern and Lagonegro basin in the Southern sector of the chain), and another shallow water carbonate platform-dominated succession deriving from the so-called “internal” or Apennine Carbonate Platform (ACP) [20–22]. During Late Aptian-Coniacian till Late Cretaceous, the ACP experienced repeated and long-lasting sub-aerial emersions, locally marked by bauxite deposits [7,8,13,23]. The various mid-upper Cretaceous stratigraphic gaps are comprised in a wide time-span, thus supporting the presence of a complex, tectonically controlled paleotopography and the long-lived exposure of some sectors of the ACP [9,18,23]. The sub-aerial exposures resulted in an intense karstification, followed by bauxite deposition [8,10,24,25]. In the Abruzzi district, two main discontinuous bauxite horizons can be recognized: a first (bx1), which is the most prominent, locally reaching 10 m of thickness, corresponds to a Late Albian-Early Cenomanian stratigraphic gap, and a second (bx2), with a maximum thickness of 1 m, bounded by Late Cenomanian-Early Turonian limestones [12,26,27]. The Cretaceous succession ends everywhere with a Paleogene gap, followed by Early Miocene sediments, consisting of limestones with Pectinidae, Bryozoa and Litotamna [12].

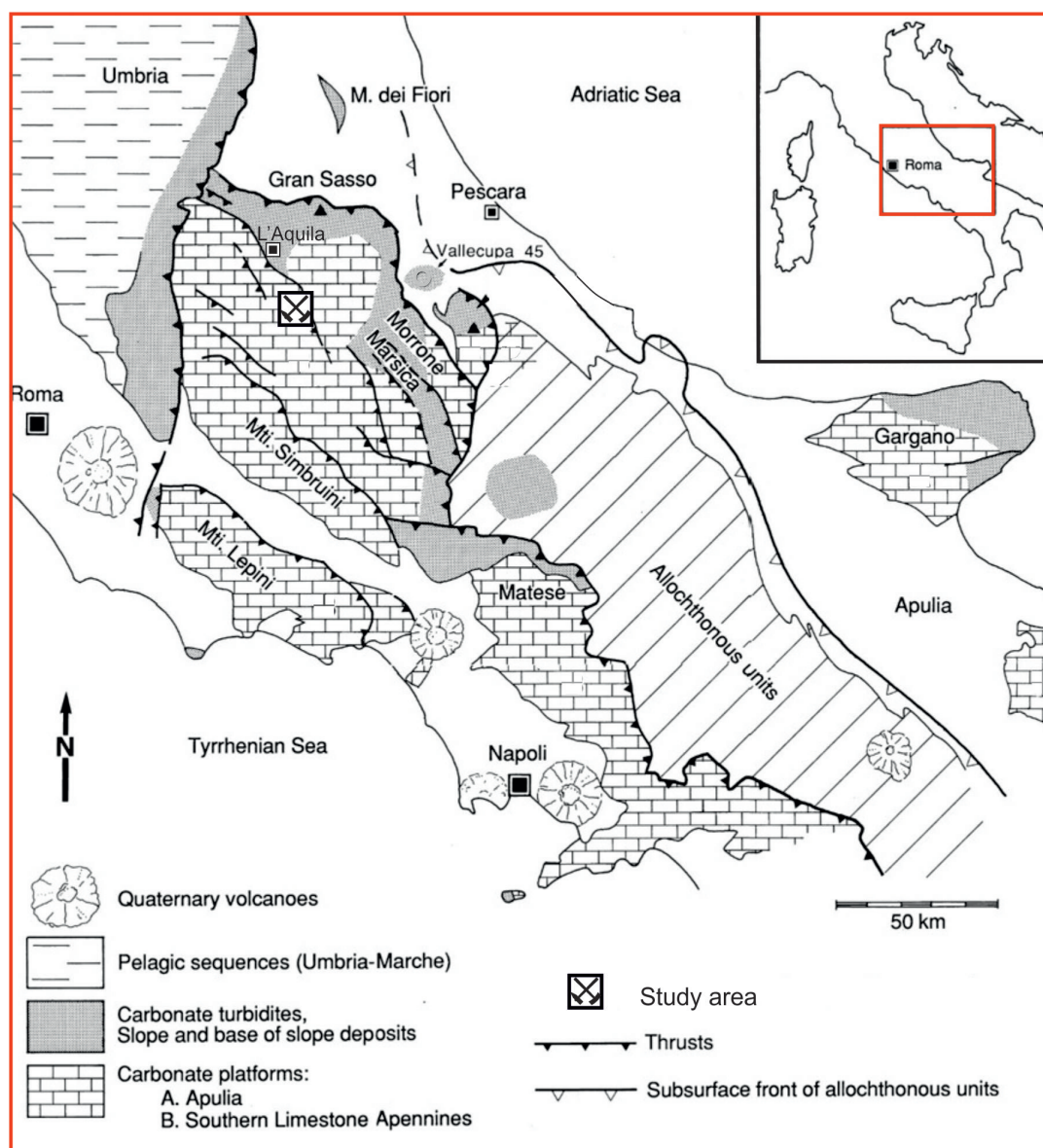


**Figure 1.** Simplified geological map of the Central and Southern Apennine chains (after [28], modified) showing the location of the study area.

### 3. Local Geology and Outcrops Description

#### 3.1. Local Geology

The bauxite outcrops considered for this study are located about 10 km south of L'Aquila city, and occur on the Campo Felice plateau and in the Monti d'Ocre area [29]. They correspond to old mine sites all established on the first and most prominent (and at the beginning of the 20th century "economic") bauxite horizon (bx1), located along the Late Albian-Early Cenomanian gap of the Mesozoic stratigraphic succession. In these sites, the stratigraphic section starts with micritic carbonates with *Dictyoconus algerianus* (Early Albian), located at the footwall of the bauxite horizon (bx1). The part of the succession on top of bauxites consists of micritic carbonate sediments and greenish marls, which are concluded by the *Cisalveolina fraasi* bio-horizon (Cenomanian). This section is followed by a carbonate breccia with bauxite matrix, which corresponds to the thinner (and "uneconomic") second bauxitic level (bx2), associated with a Late Cenomanian gap [12]. About 10 m of micritic, fenestral limestones with *Moncharmontia apenninica* and *Nummuloculina cf. irregularis* (Turonian), follow upwards.

The stratigraphic logs of the bx1 bauxite horizons [Vecchia Miniera (CFRM, Figure 2a), Mt. Orsello (CFMT, Figure 2b,c), Campo Felice (CFSW, Figure 2d,e) and Monti d'Ocre (MOC 2, Figure 2f)] are shown in Figure 2.

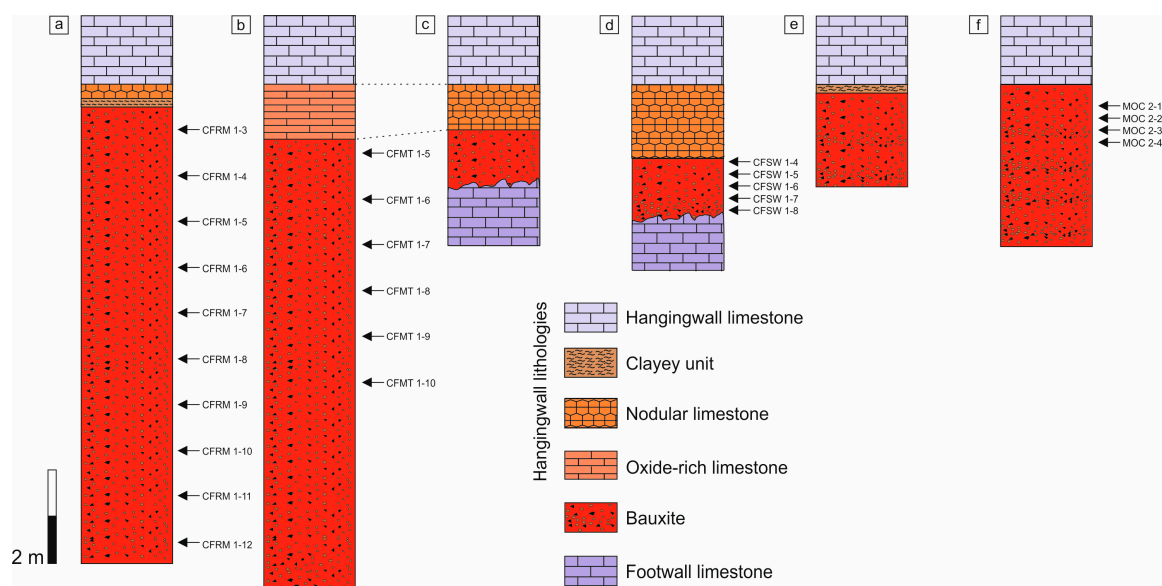


**Figure 2.** Stratigraphic logs of the bx1 bauxite horizons, with the position of the collected samples. (a) Vecchia Miniera; (b,c) Mt. Orsello; (d,e) Campo Felice; (f) Monti d'Ocre.

#### 3.2. Vecchia Miniera (CFRM)

The Vecchia Miniera outcrop is located in the NW sector of the Campo Felice plateau, and consists of a bauxitic body of lenticular shape below a limestone hangingwall (Figure 3a); the footwall contact is covered by debris and waste. The maximum thickness of the bauxite layer is 10 m (Figure 2a), while its length is about 25 m. The bauxite texture is matrix-supported, with the oolites and clasts displaying various degrees of rounding (from roughly fragmental to oolitic-pisolitic) and a medium-to-low sorting degree. The bauxite lithology shows whitish irregular patches alternated with dark red ones (Figure 3b). On the top of the ore horizon, the hangingwall starts with an ochre to reddish pelitic level, which is covered by nodular-brecciated carbonates (Figure 3c). The hangingwall limestone occurs as a white-grey lithotype.

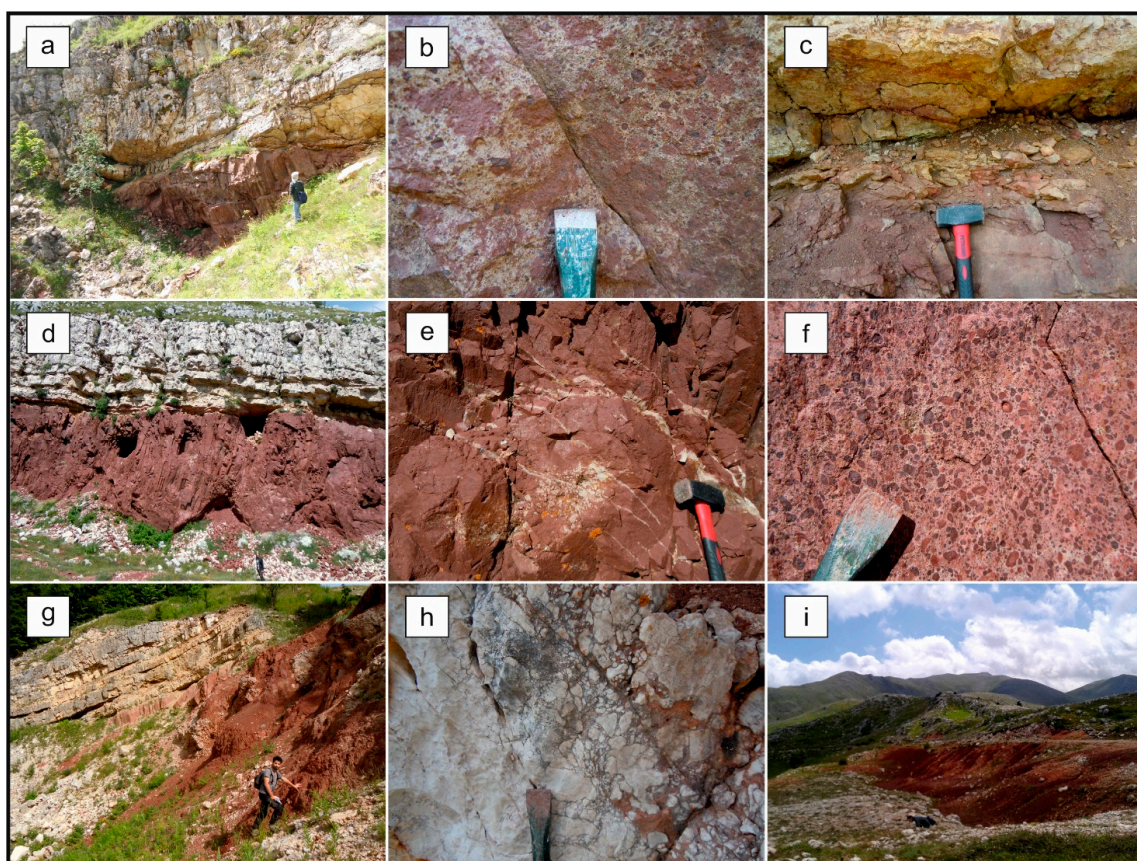


**Figure 3.** Field images of the bauxite profiles. (a) Vecchia Miniera bauxite outcrop; (b) oolitic bauxite with yellowish irregular patches (Vecchia Miniera); (c) pelite and nodular carbonate levels on top of the bauxite layer (Vecchia Miniera); (d) Mt. Orsello bauxite outcrop; (e) whitish veinlets crosscutting massive dark red bauxite (Mt. Orsello); (f) oolitic-conglomeratic bauxite (Mt. Orsello); (g) Campo Felice CFSW bauxite outcrop; (h) karstified and brecciated footwall limestone (Campo Felice CFSW); (i) Monti d'Ocre bauxite outcrop.

### 3.3. Mt. Orsello (CFMT)

Bauxite in the Mt. Orsello crops out on the SW side of the ridge carrying the same name. The dark red bauxitic lens has a maximum thickness of about 10 m (Figure 2b) and a length of 100 m (Figure 3d). The texture is matrix-supported, but in comparison with the previous outcrop there is a greater abundance of both detrital and/or oolitic-pisolitic components, with a moderately homogeneous sorting. Yellowish patches occur as at Campo Felice (Figure 3e). A matrix-supported texture is common, but the clasts are less abundant (Figure 3f). The footwall limestone is visible on the South-Eastern flank of the outcrop (Figure 2c) and shows evidence of karsting and of brittle deformation. A limestone layer follows on top of the bauxite body, showing a significant content in Fe-oxides. This calcareous layer passes laterally to ochraceous limestone (about 1 m thick, Figure 2c) with a nodular appearance. On the top of this interval there is the milky-white hangingwall limestone s.s., with evidence of brittle deformation.

### 3.4. Campo Felice (CFSW)

The Campo Felice SW outcrop is located a few km south of CFRM. In this locality, reddish soils are widespread, possibly representing the remnants of an extended bauxite horizon. The visible bauxite layer is currently about 30 m wide and 2 m thick (Figures 2d,e and 3g). At the footwall, karstified and brecciated limestone occur, characterized by infilling of reddish bauxite (Figure 3h). The hangingwall

consists of whitish, marly mudstone. In addition, another bauxite deposit occurs 3 km South-West, which due to its small size has not been sampled for this study. This tiny bauxite outcrop shows the following lithotypes from the stratigraphic bottom to the top: a 2 m thick bauxite layer, dark red in colour with lighter spots, followed by a 30 m thick clayey layer. The succession is topped by white, stratified limestone (Figure 2e).

### 3.5. Monti d'Ocre (MOC 2)

In the Monti d'Ocre outcrop (Figures 2f and 3i) the bauxite horizon has a thickness of 3 m. The bauxite ore is dark-red, with nodular zones and abundant detrital fragments. Ooides are not very abundant and the deposit mainly has a clayey lithology. In the hangingwall, below the limestone, several fossiliferous zones have been observed.

## 4. Materials and Analytical Methods

For the present study, 25 bauxite samples were collected from the Campo Felice area (CFRM, CFMT and CFSW) and from one of the small deposits of the Monti d'Ocre (MOC 2). The location of the collected samples within the studied bauxite profiles is depicted in Figure 2.

Mineralogical analyses on bauxite samples, defined mainly through X-ray powder diffraction (XRPD), were carried out on the Vecchia Miniera and Mt. Orsello prospects. In the Campo Felice and Monti d'Ocre outcrops, only isolated specimens were collected, and used for bulk geochemistry.

X-ray powder diffraction (XRPD), was carried out at the Osservatorio Vesuviano-INGV (Naples, Italy) with a PANalytical X-ray diffractometer (PANalytical, Almelo, The Netherlands), with Cu radiation  $K\alpha_1$  1.540598 Å,  $K\alpha_2$  1.54443 Å,  $K\beta$  1.39225 Å, 40 kV and 30 mA, 10 s/step and a step scan of  $0.01^\circ$   $2\theta$ . Qualitative XRD analyses were performed on all samples, using the "Xp powder" software.

Polished thin sections (~30 µm thick) were studied under petrographic microscope (transmitted and reflected light). SEM examination was carried out using a JEOL JSM 5310 instrument (JEOL, Tokyo, Japan) at the Dipartimento di Scienze della Terra, dell'Ambiente e delle Risorse (DiSTAR, Naples, Italy) and EDS microanalyses of mineral phases in thin sections were obtained by the INCA system (Oxford Instruments, Abingdon, UK), mounted on the same instrument.

Whole rock chemical analyses of major, minor and trace (including REE) elements of the bauxite samples were carried out by ACME Analytical Laboratories Ltd. (Vancouver, BC, Canada). For chemical analysis 0.5 g of each samples were leached with aqua regia, and then submitted to  $\text{LiBO}_2$  fusion and inductively coupled plasma emission (ICP-ES) spectrometer analysis for the determination of major oxides (package LF202), with minimum detection limit (M.D.M) between 0.01% and 0.04%. Loss on ignition (LOI) derives by weight difference after ignition at 1000 °C with M.D.M. = −5.1%. Rare earth and refractory elements were determined by inductively coupled plasma mass (ICP-MS) spectrometry with M.D.M. between 0.01 and 0.05 ppm.

## 5. Results

### 5.1. Mineralogy and Petrography

According to XRPD analyses (Table 1), the main oxy-hydroxides in the Vecchia Miniera and Mt. Orsello bauxites are boehmite, hematite, anatase and rutile, recorded in all the samples. Another common phase is gibbsite, which was most frequently identified in the Vecchia Miniera deposit. Other minor hydroxides are goethite and lepidocrocite, detected only at the Vecchia Miniera. A ubiquitous clay mineral in all deposits is kaolinite. Accessory minerals are calcite and illite.

The petrographic characteristics of bauxite are not significantly different between the samples taken at Vecchia Miniera and those of Mt. Orsello. The texture of the ore is mainly matrix-supported (Figure 4a), and only locally grain-supported (Figure 4b). The structure is generally oolitic (Figure 4a,b), and seldom oolitic-conglomeratic (Figure 4c,d), with rare pisolites: in fact, oolites prevail over pisolites for 50–60%. The oolites have a moderate compositional heterogeneity: part of them (from 50 up to

70%) are hematitic, and reddish brown to black (Figure 4a–d). In addition, in many cases bauxite pebbles occur as rounded clasts embedded in a whitish clayey matrix (Figure 4d) Also the bauxite matrix shows a high degree of heterogeneity, with colours ranging between dark red (Figure 4a,b) and whitish-yellow (Figure 4c,d).

**Table 1.** Qualitative XRPD analyses of the Vecchia Miniera (CFRM) and Mt. Orsello bauxites (CFRM).

Deposit	Sample ID	Bhm	Hmt	Ght	Kln	Lpd	Ant	Rtl	Gbs	Ill	Cal	
Vecchia Miniera	CFRM-1-3	O	O	O	O	O	O	O	-	-	-	
	CFRM-1-4	O	O	O	O	-	O	O	O	-	-	
	CFRM-1-5	O	O	-	O	-	O	O	O	O	-	
	CFRM-1-6	O	O	O	O	-	O	O	O	-	-	
	CFRM-1-7	O	O	-	O	-	O	O	O	-	O	
	CFRM-1-8	O	O	-	O	-	O	O	O	-	-	
	CFRM-1-9	O	O	-	O	-	O	O	O	-	-	
	CFRM-1-10	O	O	O	O	-	O	O	O	-	-	
	CFRM-1-11	O	O	O	O	-	O	O	O	-	-	
	CFRM-1-12	O	O	O	O	-	O	O	O	-	-	
	Mt. Orsello	CFMT 1-5	O	O	-	O	-	O	O	-	O	-
		CFMT 1-6	O	O	-	O	-	O	O	O	-	-
CFMT 1-7		O	O	-	O	-	O	O	-	-	-	
CFMT 1-8		O	O	-	O	-	O	O	O	-	-	
CFMT 1-10		O	O	-	O	-	O	O	-	-	O	

O = detected, - = not detected or below the detection limit; mineral abbreviations: Bhm = boehmite, Ght = goethite, Hmt = hematite, Kln = kaolinite, Lpd = lepidocrocite, Ant = anatase, Rtl = rutile, Gbs = gibbsite, Ill = illite, Cal = calcite.

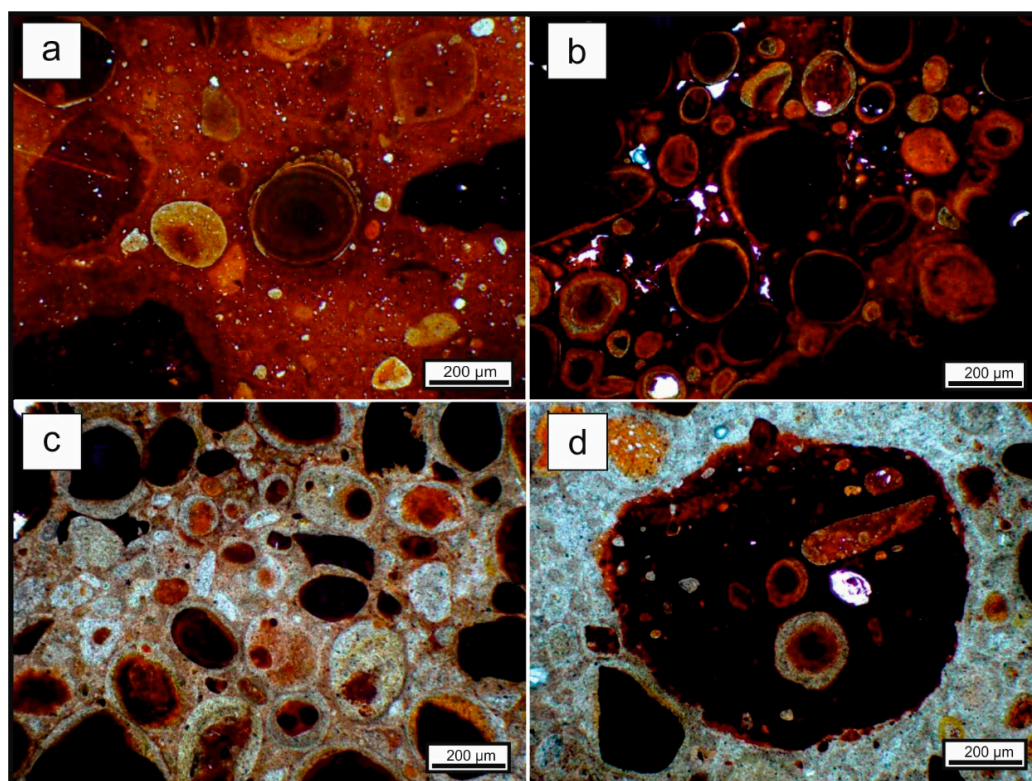


**Figure 4.** Photomicrographs with bauxite textures; (a) concentric oolites in kaolinite matrix (CFMT 1-9, Mt. Orsello); (b) grain-supported hematitic oolites (CFMT 1-8, Mt. Orsello); (c) hematitic oolites and detrital clasts in a clayey matrix (CFMT 1-5, Mt. Orsello); (d) bauxite fragment embedded in a whitish clayey matrix (CFMT 1-5, Mt. Orsello). Optical microscopy (transmitted light).

SEM images of the bauxite samples are shown in Figure 5. The oolites have a high degree of textural complexity, and in many cases, they are characterized by concentric textures, with bands of Fe-hydroxides alternated with layers of Al-hydroxides (Figure 5a). Another common feature of the oolites is shown in Figure 5b–d: an Al-hydroxide rim, likely corresponding to boehmite, which grows upon a detrital hematite core, characterizes the oolitic concretions. The matrix of the bauxite samples is mainly kaolinitic, finely inter-mixed with boehmite and/or Fe-oxy-hydroxides (Figure 5b–d). Both the oolites and the matrix enclose a wide range of fine-grained (diameter < 30  $\mu\text{m}$ ) heavy minerals such as REE-phosphates (monazite and xenotime, Figure 5e,f), ilmenite, baddeleyite, rutile, and zircon (Figure 5f–h). These phases exhibit smooth to angular surfaces and broken crystal forms, which highlight a certain degree of transport and thus their detrital origin. REEs authigenic minerals, such as fluoro-carbonate (parisite) and florencite-like phases, were also detected in cavities of the rocks (Table 2), with crystal textures ranging between massive to needle-shaped (Figure 5i).

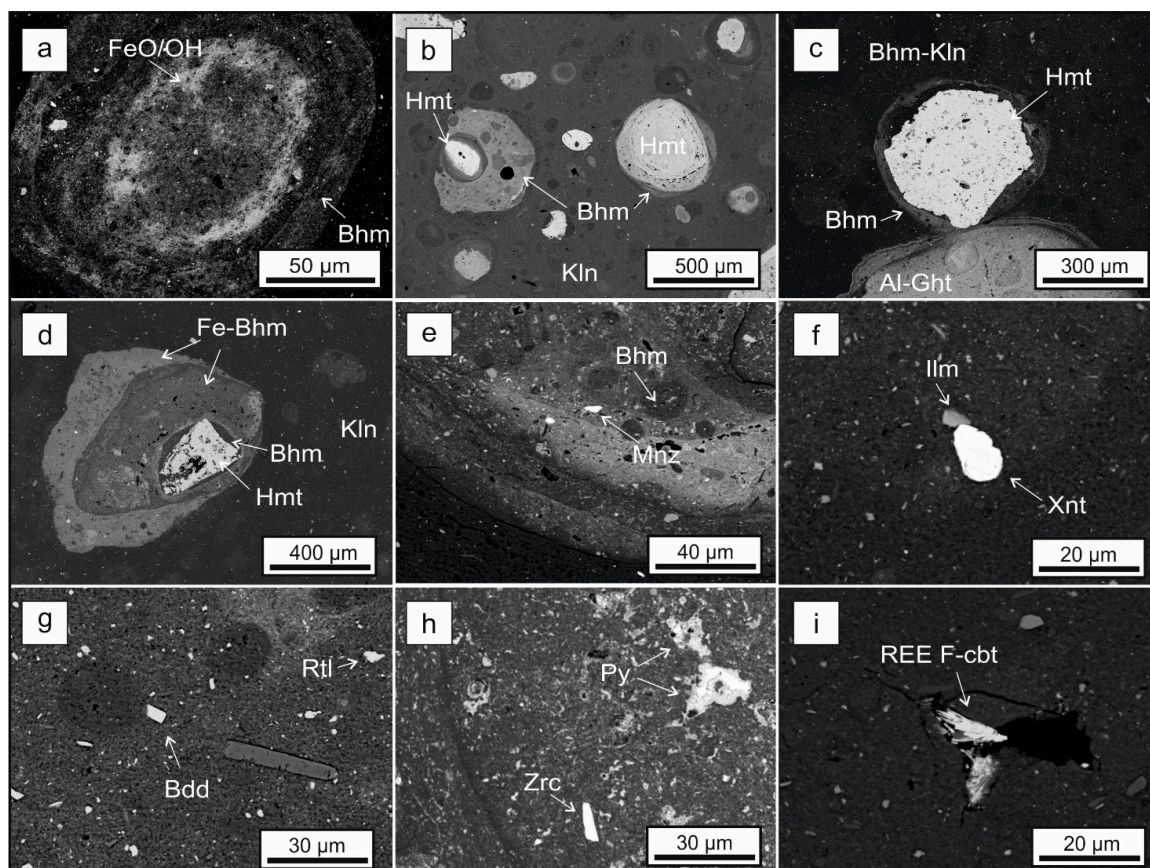


**Figure 5.** BSE (Backscattered electron) photomicrographs showing the microtexture of the oolites and the detrital minerals. (a) concentric oolite showing the alternation of Fe-(hydr)oxides with boehmite (CFMT 1-8, Mt. Orsello); (b–d) composite oolites characterized by boehmite rims growing upon hematite-rich cores (CFRM 1-9, Vecchia Miniera and CFMT 1-9, Mt. Orsello); (e) detrital monazite (Mnz) (CFMT 1-10, Mt. Orsello); (f) detrital xenotime (Xnt) and ilmenite (Ilm) embedded in a kaolinite matrix (CFRM 1-9, Vecchia Miniera); (g) detrital baddeleyite (Bdd) and rutile (Rtl) (CFRM 1-9, Vecchia Miniera); (h) authigenic pyrite (Py) encrustation and detrital zircon (Zrc) (CFMT 1-5, Mt. Orsello); (i) needle-shaped authigenic REE-fluoro-carbonate (REE F-cbt) (CFMT 1-10, Mt. Orsello).

**Table 2.** Chemical composition (EDS microanalyses) of selected REE-bearing phases observed in the bauxite samples.

Mineral	Monazite	Monazite	Xenotime	Xenotime	“Florencite”	“Florencite”	Parisite	Parisite
wt %								
F	-	-	-	-	-	-	3.07	4.25
Al <sub>2</sub> O <sub>3</sub>	0.21	0.69	2.08	0.59	19.85	21.86	0.82	2.35
SiO <sub>2</sub>	-	-	5.67	5.40	6.74	6.97	0.24	1.47
P <sub>2</sub> O <sub>5</sub>	29.73	30.48	39.48	41.05	19.82	20.23	0.26	0.07
CaO	0.40	0.86	0.40	0.39	0.91	0.90	6.85	3.45
Y <sub>2</sub> O <sub>3</sub>	-	-	45.83	45.64	-	-	1.25	0.75
La <sub>2</sub> O <sub>3</sub>	19.23	16.32	-	-	13.41	12.57	8.14	8.52
Ce <sub>2</sub> O <sub>3</sub>	32.39	33.90	0.71	-	22.82	22.32	41.31	43.30
Nd <sub>2</sub> O <sub>3</sub>	11.05	12.19	-	-	7.13	7.82	8.31	9.05
ThO <sub>2</sub>	2.39	4.14	0.87	0.93	1.23	1.10	0.27	0.71
UO <sub>2</sub>	0.42	-	-	-	-	-	-	-
CO <sub>2</sub>	-	-	-	-	-	-	23.24	24.78
Total	95.81	98.58	95.04	94.56	91.90	93.77	93.76	98.69
apfu								
F	-	-	-	-	-	-	1.84	2.38
Al	0.01	0.05	0.10	0.03	2.71	2.87	0.09	0.25
Si	-	-	0.24	0.23	0.78	0.78	0.02	0.13
P	0.74	0.73	0.71	0.75	0.97	0.95	0.01	-
Ca	0.03	0.05	0.02	0.02	0.11	0.11	0.69	0.33
Y	-	-	1.03	1.05	-	-	0.06	0.04
La	0.42	0.34	-	-	0.57	0.52	0.28	0.28
Ce	0.70	0.70	0.01	-	0.97	0.91	1.43	1.41
Nd	0.23	0.25	-	0.01	0.30	0.31	0.28	0.29
Th	0.03	0.05	0.01	0.01	0.03	0.03	0.01	0.01
U	0.01	-	-	-	-	-	-	-

- = not detected or below the detection limit.

Selected chemical microanalyses and structural formulas of the REE minerals are reported in Table 2. Cerium is the main REE in monazite, with an average Ce<sub>2</sub>O<sub>3</sub> content of 30.82 wt % (0.66 apfu Ce). Other REEs detected in monazite are La (average La<sub>2</sub>O<sub>3</sub> content = 16.30 wt %, 0.35 apfu La) and Nd (average Nd<sub>2</sub>O<sub>3</sub> content = 16.30 wt %, 0.26 apfu Nd). Xenotime has a high Y content, with average Y<sub>2</sub>O<sub>3</sub> values of 35.41 wt % (1.01 apfu Y) and shows low Ce (Ce<sub>2</sub>O<sub>3</sub> average value = 0.26 wt %, 0.01 apfu Ce) and Nd (Nd<sub>2</sub>O<sub>3</sub> average value = 0.15 wt %, 0.002 apfu Nd) concentrations. Similar to monazite, also the florencite-like phases show high Ce (Ce<sub>2</sub>O<sub>3</sub> average value = 25.72 wt %, 1.07 apfu Ce), and minor La (average La<sub>2</sub>O<sub>3</sub> content = 12.20 wt %, 0.51 apfu La) and Nd amounts (Nd<sub>2</sub>O<sub>3</sub> average value = 7.98 wt %, 0.32 apfu Nd). In regard to the chemistry of the florencite-like phases, it must be highlighted that a significant LREE (light rare earth elements) excess and a slight Al-deficiency have been detected in the Abruzzi samples, in comparison with the nominal florencite [30].

REE-fluoro-carbonates have a complex chemistry that can be mainly associated to a parisite-like composition [31]. Also, in parisite Ce (Ce<sub>2</sub>O<sub>3</sub> average value = 40.92 wt %, 1.40 apfu Ce) is the main REE, whereas Nd (Nd<sub>2</sub>O<sub>3</sub> average value = 9.34 wt %, 0.31 apfu Nd) and La (La<sub>2</sub>O<sub>3</sub> average value = 8.25 wt %, 0.29 apfu La) are less abundant. Moreover, in the analyzed parisite Ca is generally scarce (CaO average value = 4.52 wt %, 0.46 apfu Ca), if compared with the proper parisite [31]. In the latter mineral, there are also atypical traces of Al (Al<sub>2</sub>O<sub>3</sub> average value = 1.82 wt %, 0.20 apfu Al), possibly caused by the background effect of kaolinite and Al-hydroxides.

## 5.2. Major Oxides and “Bauxitophile” Elements Composition

Whole rock major and trace element concentrations of representative samples from the Vecchia Miniera, Mt. Orsello, Campo Felice and Monti d’Ocre bauxite areas are given in Table 3. As expected, the Al<sub>2</sub>O<sub>3</sub> and Fe<sub>2</sub>O<sub>3</sub> contents are high in all samples (on average, 53.84 and 21.65 wt % respectively),

while  $\text{SiO}_2$  and  $\text{TiO}_2$  have average values of 7.79 and 2.75 wt %, respectively. The  $\text{Al}_2\text{O}_3$  content of the Vecchia Miniera bauxite varies between 50.82 and 57.06 wt %, whereas in the Mt. Orsello deposit this value ranges between 50.98 and 55.91 wt %. The Campo Felice bauxite shows the highest  $\text{Al}_2\text{O}_3$  content (between 53.36 and 61.63 wt %). In the Monti d'Ocre deposits, the bauxite has an  $\text{Al}_2\text{O}_3$  content that varies between 50.58 and 51.66 wt %. In the Vecchia Miniera outcrops,  $\text{Fe}_2\text{O}_3$  values range from 11.02 to 25.15 wt %, whereas at Mt. Orsello the highest concentrations are comprised between 17.63 and 27.55 wt %. The  $\text{Fe}_2\text{O}_3$  has the lowest values in the Campo Felice deposit (between 16.22 and 20.4 wt %), whereas the  $\text{Fe}_2\text{O}_3$  content in the Monti d'Ocre varies between 23.31 and 25.09 wt %. In the Campo Felice deposit the  $\text{SiO}_2$  value is very low (about 4.2 wt %), whereas  $\text{SiO}_2$  amounts between 7.59 and 11.54 wt % have been detected in the Vecchia Miniera bauxite. In the Mt. Orsello deposit,  $\text{SiO}_2$  varies between 4.54 and 9.42 wt %, and in the Monti d'Ocre deposit  $\text{SiO}_2$  is comprised between 8.29 and 9.09 wt %. It is also important to consider that among the minor so-called “bauxitophile” elements V, Co, Ni, Cr and Zr [5], the most enriched is Cr, with an average value of 0.07 wt % (maximum value detected at Mt. Orsello –0.08 wt % and minimum in the Campo Felice bauxite –0.05 wt %). Zirconium has an average value of 510.5 ppm (with a maximum of 562.6 ppm at Campo Felice).

Nickel has an average value of 210.8 ppm and shows the highest values in the Vecchia Miniera deposit (~210–230 ppm), whereas this element is depleted in the bauxite of the Monti d'Ocre (~160–180 ppm). Vanadium shows an average value of 266.5 ppm, with concentrations slightly variable in all deposits, except for the anomalously high values of the Vecchia Miniera and Mt. Orsello bauxites (respectively 312 and 319 ppm). Cobalt has average values of 35.8 ppm.

In the diagrams of Figure 6, it can be observed that  $\text{Al}_2\text{O}_3$  and  $\text{SiO}_2$  display a negative correlation in the Campo Felice and in the Monti d'Ocre bauxites, whereas these oxides do not show any correlation in the Vecchia Miniera and Mt. Orsello deposits (Figure 6a).  $\text{Fe}_2\text{O}_3$  has a negative correlation with  $\text{Al}_2\text{O}_3$  (Figure 6b) in all deposits, with a moderate fitting of data.  $\text{TiO}_2$  has a perfect positive correlation with  $\text{Al}_2\text{O}_3$  in the whole dataset, except for an anomalous sample from Vecchia Miniera that shows a relative  $\text{TiO}_2$  depletion (Figure 6c). The  $\text{Cr}_2\text{O}_3$  values do not correlate with those of  $\text{Al}_2\text{O}_3$  (Figure 6d). In the  $\text{SiO}_2$  vs.  $\text{Al}_2\text{O}_3$  and  $\text{Cr}_2\text{O}_3$  vs.  $\text{Al}_2\text{O}_3$  correlation diagrams (Figure 6a,d, respectively), the Vecchia Miniera, Mt. Orsello and Monti d'Ocre bauxite samples are grouped in a cluster, with contrasting compositions in respect to the samples of the Campo Felice (CFSW) bauxite. This is due to the highest alumina content observed in the latter deposit.

**Table 3.** Chemical analyses of the Vecchia Miniera (CFRM), Mt. Orsello (CFRM), Campo Felice (CFSW) and Monti d’Ocre (MOC 2) bauxites.

Analyte	Unit	Vecchia Miniera										Mt. Orsello					Campo Felice					Mts D’Ocre			
		CFRM	CFRM	CFRM	CFRM	CFRM	CFRM	CFRM	CFRM	CFRM	CFRM	CFMT	CFMT	CFMT	CFMT	CFMT	CFSW	CFSW	CFSW	CFSW	CFSW	MOC	MOC	MOC	MOC
		1-4	1-5	1-6	1-8	1-9	1-10	1-11	1-12	1-5	1-6	1-7	1-8	1-9	1-10	1-4	1-5	1-6	1-7	1-8	2-1	2-2	2-3	2-4	
SiO <sub>2</sub>	wt %	11.54	7.9	8.29	7.23	7.78	8.38	7.59	7.92	5.88	7.52	4.54	7.55	9.42	8.28	4.2	5.86	6.15	10.55	8.1	9.09	8.65	8.41	8.29	
Al <sub>2</sub> O <sub>3</sub>	wt %	57.06	51.86	52.57	53.72	55.05	55.11	51.97	50.82	50.98	52.54	54.72	53.38	55.91	52.44	61.63	58.84	58.7	53.36	54.63	50.58	50.08	50.76	51.66	
Fe <sub>2</sub> O <sub>3</sub>	wt %	11.02	23.89	23.15	22.74	20.4	19.49	24.44	25.15	27.55	23.17	24.96	22.82	17.63	23.13	16.22	17.37	17.19	19.66	20.4	24.47	25.09	24.68	23.31	
MgO	wt %	0.4	0.34	0.34	0.32	0.36	0.4	0.36	0.38	0.31	0.44	0.27	0.31	0.34	0.32	0.31	0.38	0.39	0.27	0.33	0.35	0.37	0.35	0.37	
CaO	wt %	0.22	0.17	0.16	0.14	0.14	0.15	0.15	0.15	0.15	0.15	0.12	0.12	0.12	0.13	0.13	0.15	0.15	0.09	0.14	0.15	0.15	0.14	0.14	
Na <sub>2</sub> O	wt %	0.06	0.05	0.05	0.04	0.05	0.05	0.05	0.05	0.04	0.05	0.03	0.04	0.05	0.04	0.03	0.04	0.04	0.04	0.04	0.05	0.05	0.05	0.05	
K <sub>2</sub> O	wt %	0.58	0.44	0.44	0.41	0.48	0.51	0.44	0.46	0.32	0.49	0.3	0.24	0.33	0.29	0.2	0.23	0.25	0.31	0.26	0.59	0.64	0.57	0.61	
TiO <sub>2</sub>	wt %	2.62	2.64	2.63	2.8	2.89	2.82	2.65	2.62	2.55	2.82	2.81	2.68	2.79	2.66	3.16	3.13	3.12	2.74	2.86	2.41	2.59	2.6	2.66	
P <sub>2</sub> O <sub>5</sub>	wt %	0.08	0.03	0.03	0.03	0.03	0.02	0.02	0.02	0.02	0.01	<0.01	<0.01	<0.01	0.01	0.03	0.03	0.02	<0.01	0.03	0.03	0.02	0.04	0.03	
MnO	wt %	0.09	0.18	0.18	0.18	0.15	0.15	0.17	0.17	0.15	0.19	0.17	0.13	0.12	0.15	0.18	0.15	0.14	0.17	0.16	0.14	0.15	0.14	0.14	
Cr <sub>2</sub> O <sub>3</sub>	wt %	0.075	0.07	0.067	0.068	0.061	0.07	0.07	0.068	0.08	0.064	0.072	0.08	0.076	0.067	0.072	0.06	0.054	0.066	0.065	0.073	0.076	0.07	0.062	
LOI	%	15.9	12.1	11.8	12	12.3	12.5	11.8	11.9	11.7	12.3	11.7	12.4	12.9	12.2	13.5	13.5	13.5	12.5	12.7	11.8	11.8	11.9	12.4	
Ni	ppm	220	204	209	222	219	232	219	220	181	209	196	212	284	271	201	223	210	218	190	160	185	179	185	
Sc	ppm	50	62	61	60	56	57	59	62	60	59	61	58	53	60	50	52	52	51	50	59	61	61	61	
Ba	ppm	77	89	73	81	77	83	79	90	58	118	61	49	58	57	43	61	60	61	59	105	145	120	128	
Be	ppm	6	8	8	7	5	11	7	8	6	7	12	5	6	7	14	9	11	9	9	8	7	5	5	
Co	ppm	47.5	34.6	39.7	38.1	38.4	39.9	40.2	38.9	28.4	29.3	31.6	36.4	41	45.2	33.1	33.8	33.2	32.8	34	30.5	33.3	29.5	36.1	
Cs	ppm	11.7	12.2	12.4	13.5	14.9	16.7	14.9	15.7	10.7	15.1	11.9	9.1	10.2	10.8	14.3	16.9	16.7	9.7	13.4	13	16	14.8	15.5	
Ga	ppm	55.4	57.2	60.1	60.3	61.7	63.9	59.6	59.8	59.9	62.1	60.7	59	61.3	60.2	66.9	62.9	64.1	62.1	61.5	57.8	61.4	58.4	61.2	
Hf	ppm	13.8	13.1	13.4	14.5	14.6	14.1	13.9	13.5	13.6	14.3	14.4	14.1	13.6	14.1	15	15.4	15.6	14.1	15	13	14.5	13.9	14.2	
Nb	ppm	47.5	45.5	46.1	48.7	51.7	49.8	47.5	47.3	45.4	50.5	49.7	46	47.5	47.2	55.5	55.5	57.1	49.6	50.4	42.1	45.1	46.7	47.1	
Rb	ppm	38.7	37.1	39.3	41.4	49	56.5	49.5	52	28.4	52.1	33.4	25.3	32	34.3	23.9	30.4	32.4	28.8	31.3	52.7	58.3	51.9	54	
Sn	ppm	10	10	11	10	10	11	10	10	11	10	10	10	9	10	10	11	10	11	9	10	10	9	10	
Sr	ppm	49.9	64	62.9	43.3	40	39.6	37.5	41.2	35.9	36.3	26.1	29.7	31.4	29	30.8	29.4	29.7	34.2	40.8	33.7	41.1	42.1	39	
Ta	ppm	3.2	3.1	3.2	3.4	3.8	3.5	3.4	3.8	3.2	3.5	3	3.3	3.3	3.7	4	4.2	4.4	3.7	3.7	3.2	3.4	3.6	3.7	
Th	ppm	53.2	44.3	45.1	47.1	42.7	46.8	44.7	48.3	50.7	46.1	45.8	45.1	42.5	45.9	39.1	41.8	43.4	41	44.3	44.1	47.5	46.7	46.6	
U	ppm	11.2	5.1	6.3	6.1	7.2	6.8	6	5.8	5.9	6.3	5.6	5.4	11.8	5.9	7.2	8.2	7.9	5.9	6.6	3.8	4.9	5.2	5.8	
V	ppm	312	286	273	282	230	260	272	274	319	254	332	281	256	287	229	220	215	253	234	237	279	272	274	
W	ppm	5.4	5.7	5.9	5.6	5.7	5.7	5.6	5.9	6.7	6.7	5.6	6.2	5.4	6.1	6.4	7	7.9	4.8	6.2	5	5.3	5.2	4.9	
Zr	ppm	488.3	477.6	487.2	508.9	512.1	526.8	492.1	505.7	497.6	507.8	518.1	501	501	515.6	561.1	550.7	562.6	502.4	539.3	469.4	507.7	502.6	506.7	
Y	ppm	72	79	83.8	83.8	88.2	92.6	87.4	93.4	73.6	74.4	73.3	62.1	54.9	61.3	97.3	96.5	104.9	83.2	88.2	64.1	70.7	81.1	79.8	
La	ppm	197.1	145.1	149.2	149.3	138.3	159.9	139.3	139	139.3	103.6	127.6	78.8	66.8	106.7	134.3	144.5	157	122.7	129.9	98.3	112.5	107.2	113.7	
Ce	ppm	411.6	257.1	269.7	304.5	327.1	312.7	259.2	278	224.4	299.2	321.4	207.6	134.5	313.8	230.5	281.8	460.5	286.3	275.2	329.5	262	267.8	332.7	
Pr	ppm	43.5	30.94	31.26	32.24	32.28	33.98	29.91	30.71	27.15	20.71	32.3	18.34	14.81	27.15	29.03	33.44	41.15	31.66	29.61	22.06	24.31	23.18	26.39	
Nd	ppm	164.1	118.2	118.3	119.6	125.4	129.6	113.4	116	101	79.4	121.3	66.1	54.4	93	108.8	129	158.3	124.2	110.5	83	90.1	83.5	97	
Sm	ppm	27.73	20.53	21.04	21.82	23.2	23.41	20.96	21.9	17.47	15.03	23.13	14.02	10.99	18.13	19.38	23.22	30.94	25.34	20.64	16.39	17.84	17.36	19.45	
Eu	ppm	5.83	4.43	4.41	4.44	4.82	4.93	4.6	4.83	3.74	3.22	4.81	3.04	2.51	3.56	4.32	5.03	6.21	5.62	4.48	3.53	3.81	3.93	4.27	

Table 3. Cont.

		Vecchia Miniera							Mt. Orsello					Campo Felice					Mts D'Ocre					
		CFRM	CFRM	CFRM	CFRM	CFRM	CFRM	CFRM	CFMT	CFMT	CFMT	CFMT	CFMT	CFMT	CFSW	CFSW	CFSW	CFSW	CFSW	MOC	MOC	MOC	MOC	
		1-4	1-5	1-6	1-8	1-9	1-10	1-11	1-12	1-5	1-6	1-7	1-8	1-9	1-10	1-4	1-5	1-6	1-7	1-8	2-1	2-2	2-3	2-4
Gd	ppm	22.66	18.72	18.49	18.84	20.1	21.13	19.06	20.23	15.71	13.94	17.56	11.85	9.57	12.94	18.75	20.88	26	22.46	18.97	14.16	15.36	15.46	17.01
Tb	ppm	3.13	2.73	2.79	2.84	3.01	3	2.88	2.91	2.35	2.21	2.75	2.09	1.8	2.27	2.94	3.16	3.73	3.43	2.81	2.2	2.51	2.56	2.66
Dy	ppm	15.58	16.58	16.02	16.43	17.35	17.53	17.11	17.17	14.12	13.38	15.75	13.02	11.74	13.25	16.8	18.08	19.78	19.21	16.23	13.16	14.73	15.4	15.6
Ho	ppm	2.93	3.28	3.29	3.41	3.34	3.44	3.31	3.4	2.76	2.81	2.97	2.61	2.4	2.73	3.52	3.69	3.91	3.81	3.24	2.59	2.89	3.08	3.13
Er	ppm	7.81	9.18	9.65	9.54	9.6	9.58	9.73	9.79	8.28	7.98	8.85	7.97	7.65	7.84	10.33	10.59	10.65	10.42	9.73	7.65	9.09	9.15	9.06
Tm	ppm	1.21	1.44	1.4	1.45	1.48	1.47	1.48	1.48	1.27	1.28	1.37	1.26	1.21	1.34	1.57	1.64	1.64	1.62	1.43	1.2	1.39	1.35	1.41
Yb	ppm	7.65	9.06	9.25	9.4	9.66	9.48	9.1	9.67	8.38	8.15	9.33	8.84	8.2	8.64	10.2	10.99	11.13	10.45	9.52	8.22	9.44	8.97	9.39
Lu	ppm	1.13	1.39	1.42	1.45	1.5	1.44	1.4	1.49	1.27	1.29	1.43	1.35	1.27	1.36	1.59	1.61	1.68	1.65	1.45	1.24	1.43	1.38	1.42
Ce/Ce <sup>+</sup> <sub>(CN)</sub>	-	1.07	0.92	0.95	1.06	1.18	1.02	0.97	1.03	0.88	1.56	1.21	1.32	1.03	1.4	0.89	0.98	1.38	1.11	1.07	1.7	1.21	1.29	1.46
Eu/Eu <sup>+</sup> <sub>(CN)</sub>	-	0.67	0.65	0.65	0.63	0.64	0.64	0.66	0.66	0.65	0.64	0.69	0.68	0.71	0.67	0.65	0.66	0.63	0.68	0.65	0.67	0.66	0.69	0.68
(La/Yb) <sub>N(CN)</sub>	-	17.18	10.68	10.75	10.59	9.54	11.24	10.21	9.58	11.08	8.47	9.12	5.94	5.43	8.23	8.78	8.77	9.4	7.83	9.1	7.97	7.94	7.97	8.07

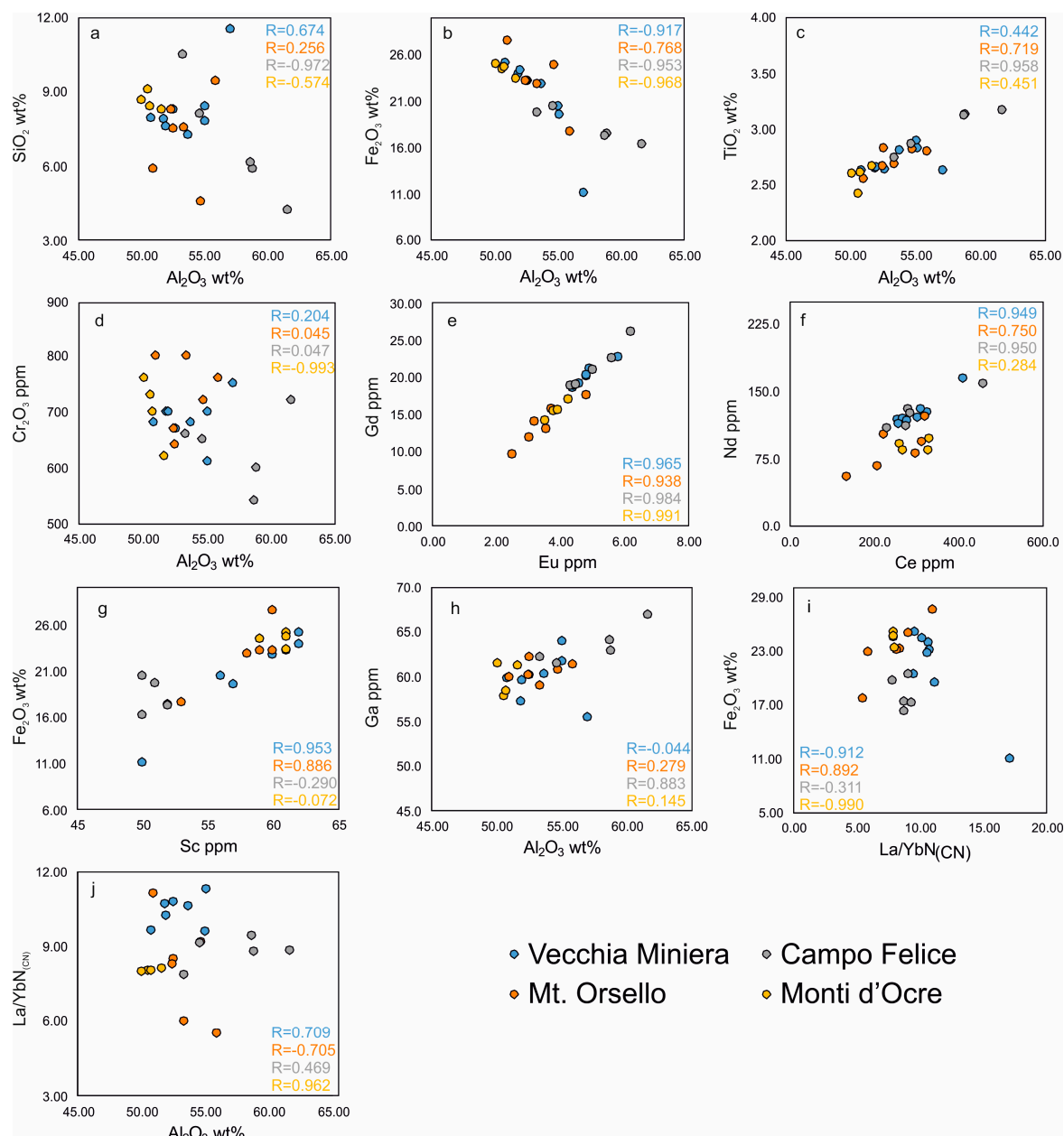


**Figure 6.** Binary plots and R values showing the correlation between the main oxides (expressed in wt %) and the trace elements (expressed in ppm). (a)  $\text{Al}_2\text{O}_3$  vs.  $\text{SiO}_2$ ; (b)  $\text{Al}_2\text{O}_3$  vs.  $\text{Fe}_2\text{O}_3$ ; (c)  $\text{Al}_2\text{O}_3$  vs.  $\text{TiO}_2$ ; (d)  $\text{Al}_2\text{O}_3$  vs.  $\text{Cr}_2\text{O}_3$ ; (e) Eu vs. Gd; (f) Ce vs. Nd; (g) Sc vs.  $\text{Fe}_2\text{O}_3$ ; (h)  $\text{Al}_2\text{O}_3$  vs. Ga; (i)  $\text{La}/\text{YbN}_{(\text{CN})}$  vs.  $\text{Fe}_2\text{O}_3$ ; (j)  $\text{Al}_2\text{O}_3$  vs.  $\text{La}/\text{YbN}_{(\text{CN})}$ .

### 5.3. High-Tech Metals (REEs, Sc and Ga) Geochemistry

The total REEs amounts are strongly variable in the considered Abruzzi bauxites, with the highest concentrations observed in the Vecchia Miniera and in the Campo Felice (CFSW) deposits (REEs average values = 704 and 702 ppm respectively), whereas a sharp REEs-depletion characterizes the Monti d'Ocre and Mt. Orsello mining sites (REEs average values = 596 and 534 ppm respectively). The most abundant element among the REEs is Ce, which displays the highest values in the Campo Felice and Vecchia Miniera deposits, where its amount is of 306 and 302 ppm on average respectively. A sharp decrease in Ce concentration is observed in the Monti d'Ocre and Mt. Orsello bauxites (Ce average values = 298 and 224 ppm respectively). Positive correlations are visible in the Eu vs. Gd and

Ce vs. Nd diagrams (Figure 6e,f). The positive correlation between Eu and Gd is characterized by a high fitting of data, with an almost constant Eu/Gd ratio. In contrast, even though Ce and Nd show a positive correlation, these elements have a more variable ratio.

The Sc and Ga concentrations are quite constant in all the studied bauxite profiles with average values of 57 and 60 ppm respectively. Scandium shows a positive correlation with  $\text{Fe}_2\text{O}_3$  only in the Vecchia Miniera and Mt. Orsello deposits (Figure 6g). Gallium has a very moderate positive correlation with  $\text{Al}_2\text{O}_3$  in the Mt. Orsello and Monti d’Ocre deposits, whereas it is strongly positively correlated with the latter oxide in the Campo Felice bauxite (Figure 6h).

The chondrite normalized (CN) patterns shown in Figure 7 display enrichment in LREE (La, Ce, Pr, Nd) relative to MREE (medium rare earth elements: Sm, Eu, Gd, Y, Tb, Dy) and HREE (heavy rare earth elements: Ho, Er, Tm, Yb, Lu) and flat segments for MREE and HREE. The LREE to HREE enrichment, monitored with the  $\text{La}/\text{Yb}_{(\text{CN})}$  ratio, is higher in the Vecchia Miniera bauxite (average  $\text{La}/\text{Yb}_{(\text{CN})}$  value = 11.22), where it reaches the positive peak value in the uppermost sample of the profile (CFRM 1-4,  $\text{La}/\text{Yb}_{(\text{CN})}$  value = 17.18). In the Mt. Orsello, Campo Felice and Monti d’Ocre deposits the  $\text{La}/\text{Yb}_{(\text{CN})}$  ratios are very similar, with 8.05, 8.77 and 7.99 respective average values. Nevertheless, the  $\text{La}/\text{Yb}_{(\text{CN})}$  range of values shows a remarkable difference. In fact, this index varies in a narrow range in the Monti d’Ocre and in the Campo Felice bauxite (7.44–9.07 and 7.43–9.40 respectively). In contrast, at Mt. Orsello the  $\text{La}/\text{Yb}_{(\text{CN})}$  ratio has not only a broader variation ( $\text{La}/\text{Yb}_{(\text{CN})}$  range values = 5.43–11.08) but shows also a progressive increase in the uppermost samples of the profile (as at Vecchia Miniera).

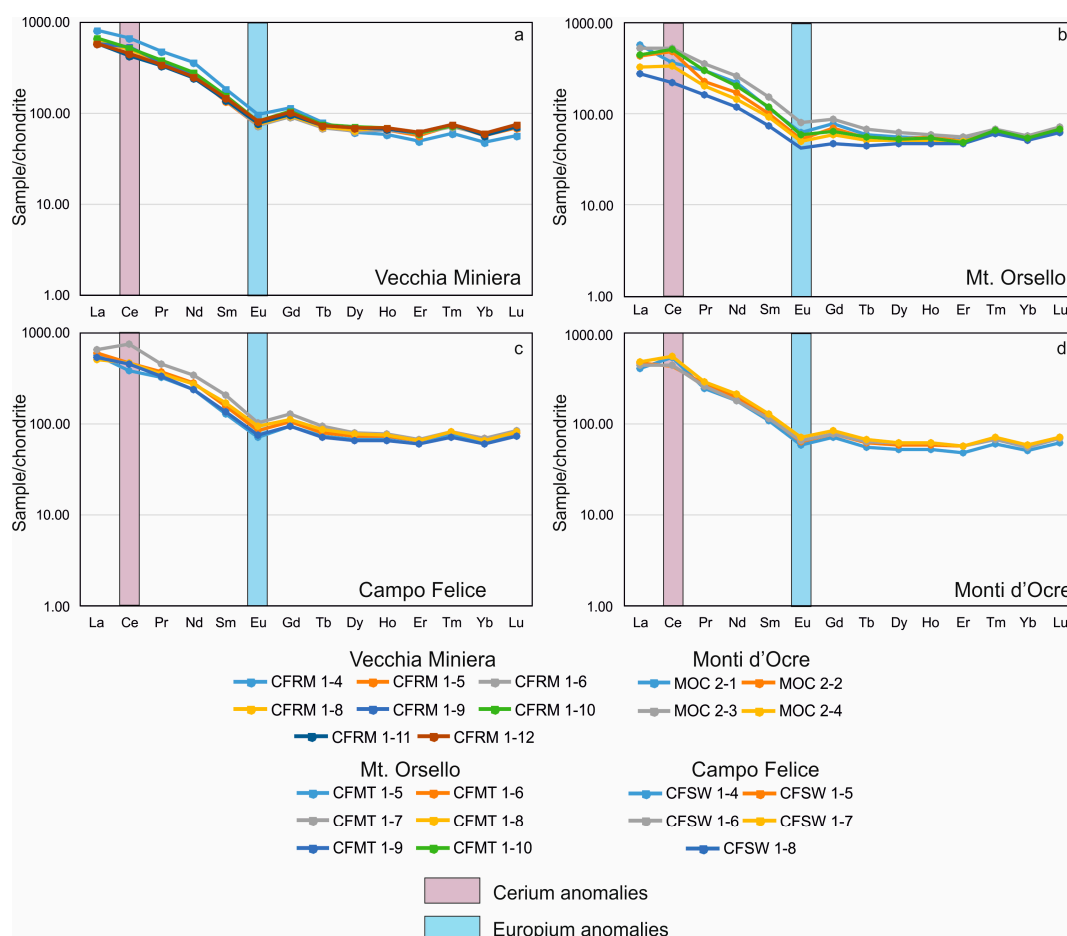


**Figure 7.** REE/chondrite normalized patterns (the chondrite reference values are taken from [32]). (a) Vecchia Miniera; (b) Mt. Orsello; (c) Campo Felice; (d) Monti d’Ocre.

In Figure 6i, a comparison between the  $\text{La}/\text{YbN}_{(\text{CN})}$  ratio and the  $\text{Fe}_2\text{O}_3$  content of the studied bauxites is reported. In the binary plot, the majority of data do not show a particular relationship, except for the Mt. Orsello deposit, in which a moderate positive correlation is visible between the  $\text{Fe}_2\text{O}_3$  content and the  $\text{La}/\text{YbN}_{(\text{CN})}$  index. Moreover, the  $\text{La}/\text{YbN}_{(\text{CN})}$  ratio displays an interesting relationship also with  $\text{Al}_2\text{O}_3$  (Figure 6j). In particular, in the Vecchia Miniera and Monti d'Ocre bauxites positive correlations with good fitting are visible, whereas an irregular, though positive correlation characterizes the Campo Felice deposit. Lastly, the  $\text{Al}_2\text{O}_3$  content and the  $\text{La}/\text{YbN}_{(\text{CN})}$  ratio are negatively correlated in the Mt. Orsello bauxite.

Cerium and Eu anomalies are very common in the Abruzzi bauxite. These anomalies are shown through the  $\text{Ce}/\text{Ce}^*$  and  $\text{Eu}/\text{Eu}^*$  ratio (Figure 8a–d). Cerium anomalies occur in the Mt. Orsello, Campo Felice and in the Monti d'Ocre deposits, whereas in the Vecchia Miniera bauxite Ce has no remarkable anomalies. However, the  $\text{Ce}/\text{Ce}^*$  index varies broadly in the studied deposits (Figure 8a–d), with values ranging between 0.88 and 1.70, reflecting the occurrence of both positive and negative anomalies. Europium produces constant negative anomalies in the samples of the studied deposits (Figures 7 and 8), with  $\text{Eu}/\text{Eu}^*$  ratios narrowed between 0.63 and 0.71.

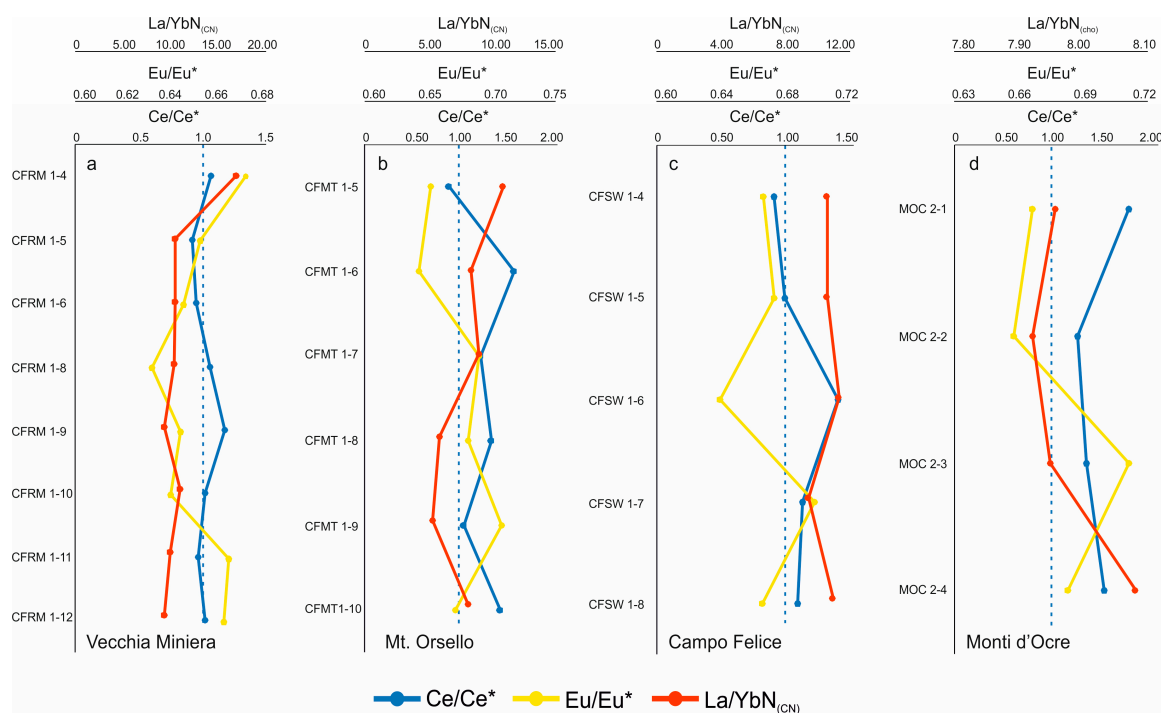


**Figure 8.**  $\text{Ce}/\text{Ce}^*$ ,  $\text{Eu}/\text{Eu}^*$  and  $\text{La}/\text{Yb}$  geochemical logs. (a) Vecchia Miniera; (b) Mt. Orsello; (c) Campo Felice; (d) Monti d'Ocre. The  $\text{Ce}/\text{Ce}^*$  and  $\text{Eu}/\text{Eu}^*$  anomalies have been quantified following the formulae proposed by [33]. The blue dashed lines stand for  $\text{Ce}/\text{Ce}^* = 1$ .

## 6. Discussion

### 6.1. Genetic Process

The ore textures of the Abruzzi bauxites that vary between oolitic and oolitic-conglomeratic in all deposits, the presence of several grains/pebbles of older bauxite, as well as the angular fragments of hematite-goethite among the ooids, as already suggested by [7,29], corroborate the fact that the bauxite horizons currently in place are derived from the erosion and re-sedimentation of older bauxites and possibly also from eroded duricrusts, formed on the exposed carbonate platform. Moreover, the Fe-rich oolites and fragments commonly display an Al-hydroxide rich rim, which suggest a certain degree of in situ weathering that occurred after the reworking of the older bauxite-duricrust. Other features that

highlight the occurrence of in situ alteration processes affecting the Abruzzi bauxites are the negative correlations between  $\text{Al}_2\text{O}_3$  and  $\text{SiO}_2$  and  $\text{Al}_2\text{O}_3$  and  $\text{Fe}_2\text{O}_3$ , and the positive correlation between  $\text{Al}_2\text{O}_3$  and  $\text{TiO}_2$ . These geochemical tendencies suggest that a significant leaching of silica and the concentration of more immobile elements such as Al, Fe and Ti occurred after the resedimentation of the old bauxitic material in karst cavities [8].

The amounts of “bauxitophile” elements (Cr, Ni, V, Co, and Zr) are similar in all the studied deposits. Nickel and Co, which are elsewhere associated with parent rocks of basic affinity [8,33], have low concentrations in the Abruzzi bauxites. Vanadium occurs in normal amounts, although in some cases there are anomalies, probably derived from V-rich detrital minerals from the source rock. Detrital zircon and baddeleyite are responsible for the relatively high Zr concentration in the bauxite ore.

The REE amounts are generally constant in all Abruzzi deposits, except for a relative enrichment in the Campo Felice and Vecchia Miniera bauxites: the latter is the only deposit where we have detected a sample characterized by a very high  $\text{La}/\text{YbN}_{(\text{CN})}$  ratio. Moreover, even though in the Vecchia Miniera deposit the Ce anomalies are less marked likely as a result of a corresponding high La and Pr enrichment, the  $\text{Ce}/\text{Ce}^*$  ratio is  $>1$ . The detection in the Abruzzi bauxites of authigenic LREE-minerals, such as the REE fluoro-carbonates and florencite, that are also common to most bauxite deposits of the world [11,34–39], evidences that REEs were partially solubilized and mobilized from their “precursor” minerals, specifically detrital monazite (or other minor REEs-bearing minerals), and re-precipitated in new supergene phases. In fact, although the analysed monazites do not show clear textural evidences of chemical weathering, recent experimental works [40] have shown that oxidizing fluids are able to produce dissolution processes, generating lanthanides (mostly LREE) remobilization and favouring their subsequent uptaking in secondary phases. Monazite dissolution is controlled by the occurrence of U traces, as the oxidation of this element from the tetravalent ( $\text{U}^{4+}$ ) to the hexavalent ( $\text{U}^{6+}$ ) state strongly weakens the crystal lattice of such phosphate [41]. In fact, the monazites occurring in the Abruzzi bauxites show trace amounts of U, with a  $\text{U}_2\text{O}_3$  average value of 0.48 wt %, which could have favoured their dissolution. The precipitation of REE-fluoro-carbonates takes place under alkaline conditions, likely provided by the interaction between the groundwater and the footwall/hangingwall limestone [33,42,43]. During this process the Ce oxidation from the trivalent ( $\text{Ce}^{3+}$ ) to the tetravalent ( $\text{Ce}^{4+}$ ) state, plays an important role to favour the LREEs retainment in the newly formed supergene (and more stable) REE phases [43,44].

Another proxy showing the REE remobilization during bauxitization is their high-to-moderate correlation between REE concentrations and  $\text{Al}_2\text{O}_3$  amounts, which suggests the enrichment of REE during the progressive formation of Al-hydroxides after in-situ weathering of the precursor materials filling the karst cavities. A remarkable exception in the  $\text{Al}_2\text{O}_3$ - $\text{La}/\text{YbN}_{(\text{CN})}$  relationship is the Mt. Orsello deposit, where a steep negative correlation was observed, and the  $\text{La}/\text{YbN}_{(\text{CN})}$  is positively correlated with  $\text{Fe}_2\text{O}_3$ , suggesting a major role of Fe-(hydr)oxides in the uptaking of LREEs [45–47].

Recent works successfully showed that the mineralogy of and geochemistry of REE can be controlled by the variation of pH and Eh [38], which can occur during several ore-forming stages that characterize the genesis of karst bauxites [38,48]. For example, in the Permian Longhe and Tianyang bauxite deposits (China) the in situ bauxitization was characterized by an alkaline and oxidizing environment ( $7 < \text{pH} < 10$ ,  $-0.8 < \text{Eh} < 0$ , [42,49]). Under these conditions, a classic enrichment in LREE and a depletion in HREE resulted in the precipitation of LREE-bearing fluoro-carbonates. In contrast, during the quaternary reworking of the bauxite in the karst networks, the strong pH and Eh variation triggered the LREE-fluoro-carbonates dissolution and, as a consequence, a significant decrease of the LREE/HREE ratio in the newly formed bauxite deposits [38]. Also, in the Abruzzi bauxite case study, the deposits likely underwent a multistage evolution that involved lateritization, erosion and reworking, and a relatively later bauxitization in situ also occurred in the karst networks. However, by taking into account that the observed REE secondary phases are present as open spaces infilling, it is possible to infer that the chemical weathering stage in the karst networks was the main factor controlling the current REE mineralogy and chemistry in the studied deposits.

Even though Sc and Ga have relatively low average concentrations in the Abruzzi bauxite (57 and 60 ppm respectively), their geochemical trends provide interesting insights. In fact, Sc displays moderately positive correlations with  $\text{Fe}_2\text{O}_3$ , whereas Ga is positively correlated with  $\text{Al}_2\text{O}_3$  (Figure 6g,h). Considering the existing negative correlation between  $\text{Fe}_2\text{O}_3$  and  $\text{Al}_2\text{O}_3$  (Figure 6b), it is evident that a significant geochemical (and possibly mineralogical) decoupling has occurred between Sc and Ga during the bauxitization process. The geochemical affinity of Sc with  $\text{Fe}_2\text{O}_3$  has been considered to a great extent both in bauxites and in laterites. Many authors [50–52] proposed that the Sc occurrence in residual soils is mainly related to an isomorphous substitution of  $\text{Sc}^{3+}$  with  $\text{Fe}^{3+}$  in the hematite lattice and lesser with the  $\text{Sc}^{3+}$  uptaking as adsorbed metal onto the goethite surface. The behaviour of Ga during the bauxitization process could be variable. In particular, the Ga solubility depends on the pH of the soil solutions [53–56], which in turn define the Ga speciation in Al- or Fe-hydroxides. As shown by [56], the Ga enrichment in Fe-(hydr)oxides requires a sharp physico-chemical variation of the soil solution towards very low pH values (<4). In the specific case of the studied bauxites, the correlation between Ga and  $\text{Al}_2\text{O}_3$  displays a steady ratio, thus pointing to constant pH conditions (pH > 4) during the bauxitization process.

## 6.2. Comparison with other Bauxite Deposits of the Tethyan Realm

The comparison between the chemistry of the major oxides of the Abruzzi deposits with those measured in other important Mediterranean bauxites (Figure 9a–f) has revealed some interesting features. The chemical composition of the bauxites in the Abruzzi district has been compared with other bauxites from the major districts of the circum-Mediterranean area: Spinazzola (Apulia) [42], Salento and Gargano (Apulia) [11,57], Nurra (Sardinia) [44], Matese Mts. and Caserta districts (Campania) [8, 10], Bolkardagi (Turkey) [58], Mortas (Turkey) [59] and the Parnassos-Ghiona district (Greece) [60].

In the  $\text{Al}_2\text{O}_3$  vs.  $\text{SiO}_2$  (Figure 9a) diagram, the Abruzzi bauxites (about  $\text{Al}_2\text{O}_3$  50–60%,  $\text{SiO}_2$  5–10%) are located in an area of the diagram also covered by the compositions of the majority of the other Mediterranean districts (45–65%  $\text{Al}_2\text{O}_3$ ,  $\text{SiO}_2$  1–12% approximately), with the exception of the Spinazzola (Apulia) bauxites, which form a cluster of values relatively enriched in  $\text{SiO}_2$  (about 7–22%) and depleted in  $\text{Al}_2\text{O}_3$  (about 40–55%). Also, the Nurra (Sardinia) bauxite deviates from the other considered districts, presenting a wider range of values with  $\text{Al}_2\text{O}_3$  between 40% and 70%, and  $\text{SiO}_2$  between 2% and 38%. However, the  $\text{SiO}_2$  enrichment of the Sardinia bauxites is considered to be due to the alteration process caused by the circulation of Si-rich solutions, which caused the re-silicification of boehmite as a consequence of the emplacement of Tertiary volcanites on top of the bauxites [61]. Lastly, the Salento (Apulia) bauxites [57] display a significant deficiency of  $\text{SiO}_2$ , whose values range between 0.44 and 0.10 wt %  $\text{SiO}_2$ .

The Abruzzi bauxites have a  $\text{Fe}_2\text{O}_3$  content similar to other Italian bauxites (Figure 9b). Notable exceptions are the Nurra ones, where  $\text{Fe}_2\text{O}_3$  has a range of values on average lower (about 2–18 wt %), and the bauxites of the Caserta district (Campania), where  $\text{Fe}_2\text{O}_3$  is on average higher (about 15–40 wt %). The  $\text{TiO}_2$  (Figure 9c) content of the Abruzzi bauxites is similar to the amounts measured in other Mediterranean districts (about 1.9–3.2 wt %). The only exceptions are the Spinazzola and Gargano (Apulia) deposit, which are on average richer in  $\text{TiO}_2$  with values between 3.5–4.5 wt % and 2.4–5.4 wt % respectively. In the  $\text{Al}_2\text{O}_3$  vs.  $\text{Cr}_2\text{O}_3$  binary plot (Figure 9d) the Abruzzi bauxites as well as the majority of the Mediterranean deposits plot in a composition field comprised between 32–75 wt %  $\text{Al}_2\text{O}_3$  and 300–1200 ppm  $\text{Cr}_2\text{O}_3$ . The only remarkable exception is the Salento (Apulia) bauxite, which is characterized by significantly higher Cr amount ( $\text{Cr}_2\text{O}_3$  range of values: 1340–1650 ppm). In the  $\text{Cr}_2\text{O}_3$  vs. Ni diagram (Figure 9e) the Abruzzi bauxites form a well-defined cluster, with restricted values (Ni about 150–300 ppm, Cr about 380–550 ppm). The Spinazzola bauxite (Apulia) displays not only a major enrichment in these two elements, but also a greater dispersion of the data (Ni about 270–600 ppm, Cr about 500–920 ppm). Some of the Cr values of the Nurra bauxites deviate partially from the average values (about 630 to 880 ppm). Greek bauxites have much higher values, both for Cr (700–1200 ppm approximately) and Ni (about 450–700 ppm). Moreover, as above remarked in

Figure 9e, also the Gargano (Apulia) bauxite shows distinctive composition with higher Cr amount. The relative high concentration of  $\text{Cr}_2\text{O}_3$  and the Ni amounts detected in the Parnassos-Ghiona (Greece), and Spinazzola (Apulia) deposits may be a significant proxy of a partial contribution of mafic/ultramafic lithologies (likely corresponding to Tethys ophiolitic suites) for the bauxite source material [64].

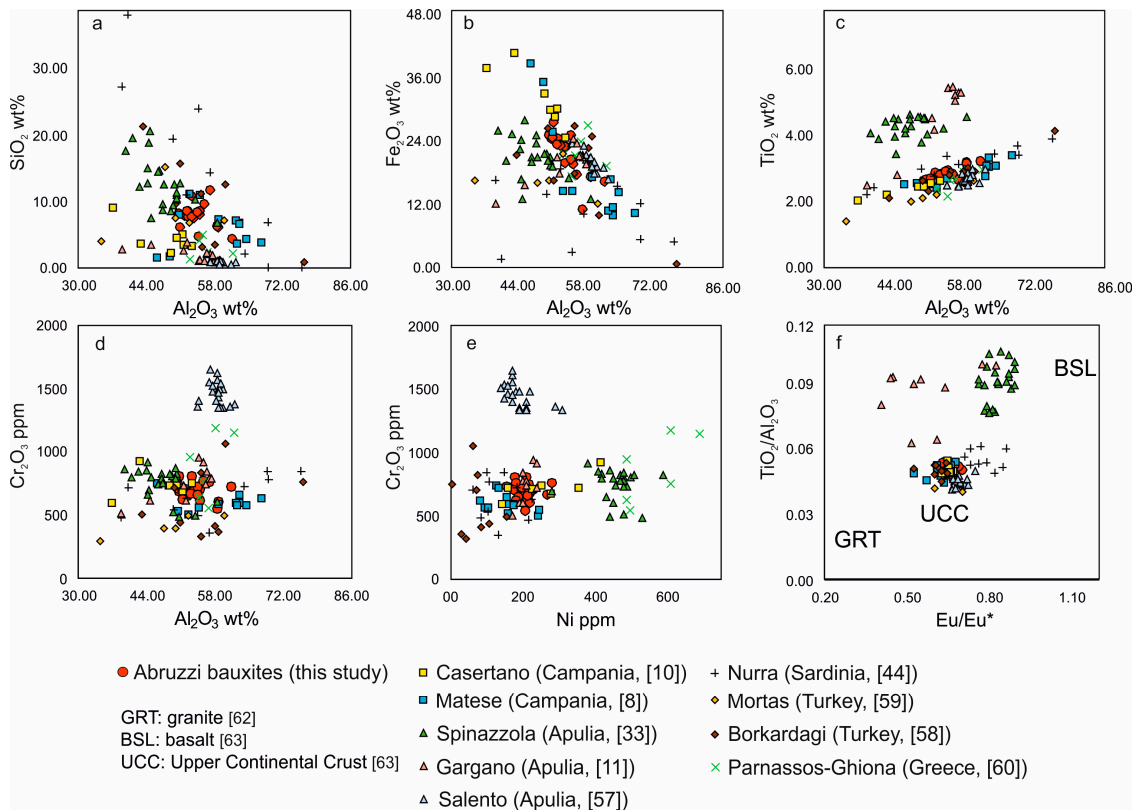


**Figure 9.** Binary plots comparing the chemistry of the Abruzzi bauxites to that of other bauxites in the Mediterranean realm. (a)  $\text{Al}_2\text{O}_3$  vs.  $\text{SiO}_2$ ; (b)  $\text{Al}_2\text{O}_3$  vs.  $\text{Fe}_2\text{O}_3$ ; (c)  $\text{Al}_2\text{O}_3$  vs.  $\text{TiO}_2$ ; (d)  $\text{Al}_2\text{O}_3$  vs.  $\text{Cr}_2\text{O}_3$ ; (e) Ni vs. Cr; (f)  $\text{Eu}/\text{Eu}^*$  vs.  $\text{TiO}_2/\text{Al}_2\text{O}_3$  (references are indicated in the plot legend, GRT [62], BSL and UCC [63]). **N.B.:** in the Ni vs.  $\text{Cr}_2\text{O}_3$  and in the  $\text{TiO}_2/\text{Al}_2\text{O}_3$  vs.  $\text{Eu}/\text{Eu}^*$  binary plots the geochemistry of the Mortas (Turkey, [59]) and Parnassos-Ghiona (Greece, [60]) deposits has not been reported due to the absence of data in the original papers.

To better constrain the analogies and differences between the Abruzzi bauxites and several others from the Mediterranean area, their compositions have been plotted in the whole rock  $\text{Al}_2\text{O}_3$ - $\text{SiO}_2$ - $\text{Fe}_2\text{O}_3$ (t) ternary plot [5] (Figure 10). The chemistry of the major elements defines the Abruzzi bauxites in a field between bauxites s.s. and Fe-rich bauxites. Also, the Casertano and Matese bauxites (Campania district, Italy) plot within the same field, but they are characterized by a broader range of  $\text{Al}_2\text{O}_3$  and  $\text{Fe}_2\text{O}_3$  values, and by a slight lower  $\text{SiO}_2$  concentration. The Nurra (Sardinia, Italy) bauxites show a wider chemical variability as their samples fall in the field comprising low-Fe bauxite, bauxite s.s. and clayey bauxite. In general, in comparison with the Abruzzi district, the Nurra bauxite is characterized by higher  $\text{Al}_2\text{O}_3$  and  $\text{SiO}_2$  concentration and by much less  $\text{Fe}_2\text{O}_3$ . The Apulia (Spinazzola-Murge, Gargano and Salento, Italy) deposits form two discrete clusters of data. The Salento and Gargano bauxites have a similar chemistry, with the exception of few samples from the Gargano deposit that show a relatively higher  $\text{SiO}_2$  concentration. The chemistry of these deposits falls along the limit between bauxites s.s. and Fe-rich bauxites. In comparison with the Abruzzi district, the Salento and Gargano bauxites are characterized by fairly similar  $\text{Al}_2\text{O}_3$  and  $\text{Fe}_2\text{O}_3$  concentrations, and by scarce  $\text{SiO}_2$ . Also, the chemistry of the Spinazzola deposit occurs within the same field of other

Apulian bauxites, with the exception of few samples, which plot at the limit with the clayey bauxite field due to their higher  $\text{SiO}_2$  concentration. In general, the Spinazzola bauxite has similar  $\text{Al}_2\text{O}_3$  and  $\text{Fe}_2\text{O}_3$  concentration to those of the Abruzzi deposits, but displays a net  $\text{SiO}_2$  enrichment.

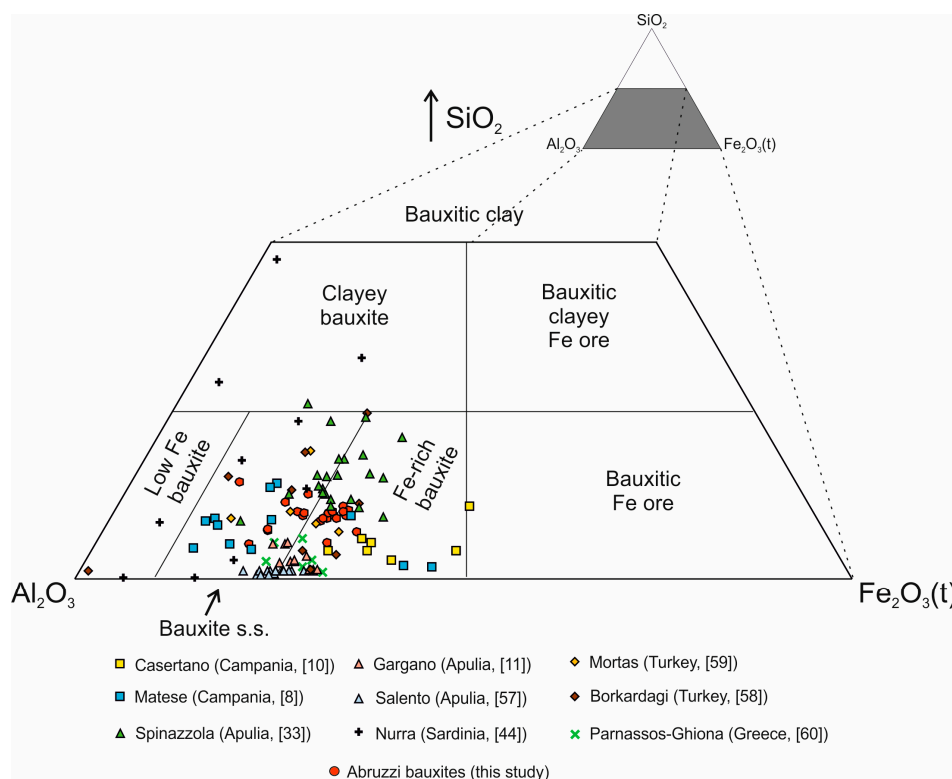


**Figure 10.**  $\text{Al}_2\text{O}_3$ - $\text{SiO}_2$ - $\text{Fe}_2\text{O}_3(t)$  ternary plot (classification fields from [5]) of the Abruzzi bauxites and the other districts of the Mediterranean realm (references are indicated in the plot legend).

The Parnassos-Ghiona (Greece) bauxite shows an intermediate composition between the Abruzzi and the Gargano-Salento deposits. In particular, the Parnassos-Ghiona bauxite has similar  $\text{Al}_2\text{O}_3$  and  $\text{Fe}_2\text{O}_3$  values as those of the Apulian bauxites, but displays a  $\text{SiO}_2$  concentration that is intermediate between those of Abruzzi and the Gargano-Salento deposits. Lastly, the Turkish bauxites (Mortas and Borkardagi) have a chemical composition fairly similar to that of the Abruzzi deposits, with the exception of few samples measured at Borkardagi. In particular, despite the majority of data of the Borkardagi bauxite fall in the bauxite s.s. and in the Fe-rich bauxite fields, few samples display a relative  $\text{SiO}_2$  enrichment in comparison with the Abruzzi district, and thus plot towards the limit with the clayey bauxite field. Moreover, a sample from Borkardagi shows remarkable  $\text{Al}_2\text{O}_3$  enrichment paired with  $\text{SiO}_2$  and  $\text{Fe}_2\text{O}_3$  depletion, and plots in the low-Fe bauxite field.

In conclusion, the Abruzzi bauxites are very similar in the chemical composition of their major elements to other Mediterranean bauxite ores, but are distinctly different from the Apulian and Sardinian deposits.

### 6.3. Parental Affinity of the Bauxite

While lateritic bauxites can be directly related, through their textures and composition, to the underlying source rocks [1], this is rarely the case for bauxites occurring above carbonate sequences (karst bauxites). The origin of the parent material for the karst bauxites in Central and Southern Apennines is a matter of debate, essentially because the carbonate platform hosting these deposits is considered to have remained of the “Bahamian”-type for all the Mesozoic, precluded to any direct input of siliciclastic marine or fluvial sedimentation before and during bauxite formation [65–67].

For this reason, there was a strong “historical” feeling that the Apennine bauxites were possibly originated from windblown pyroclastic materials that covered the carbonate platforms and were then subjected to in situ lateritization and local remobilization [7,23], as it is the case of Jamaican bauxites [68].

This hypothesis was confirmed by the dating of zircons contained in Matese bauxite [9], which in part resulted to have Cretaceous ages (ca. 90 Ma) as the host bauxites, finally testifying that part of the source material consisted of pyroclastic ashes derived from a volcanism coeval with the formation of bauxites [9]. At the same time, the additional occurrence of zircons with Pan-African ages do not exclude that part of the parent material consisted of eolian sands carried by winds from the African craton, in a similar way to the modern Saharan eolian dust, which is transported to great distances in Europe and also in North America [69]. The discovery of fine-grained detrital minerals in the Abruzzi bauxites (e.g., zircon, ilmenite, rutile, baddeleyite) supports a similar origin also for the parent material of the Abruzzi bauxite. However, we could not technically confirm beyond doubt the previous dating, because in the Abruzzi bauxites no measurable zircons were found so far.

During the bauxitization process, a fractionation of major, minor and trace elements, including REEs, takes place. Some ratios, especially the  $\text{Eu}/\text{Eu}^*$  have proved, however, to be retained during intense weathering phenomena [44]. In all the Abruzzi deposits considered, the  $\text{Eu}/\text{Eu}^*$  ratio shows negligible changes ( $0.67 < \text{Eu}/\text{Eu}^* < 0.72$ ; Figure 8). Moreover, the values of the  $\text{Eu}/\text{Eu}^*$  ratio are very similar to those calculated by [8] for the bauxites in the Matese Mts. Another insight into the possible source of the parent material for the Abruzzi deposits could be also derived from the diagram of Figure 9e, with its Ni and Cr contents compared with those of other Mediterranean karst bauxite ores [70]. It was observed that the Abruzzi bauxites have Ni-Cr contents very similar to those of Turkish [58,59], Sardinian [44] and Matese Mts. bauxites [8], but much lower than those detected in most Greek bauxites [60]. This depends on the lack in other deposits of the Mediterranean realm of the basic protore signature shared by the Greek bauxites, which lie above or nearby ophiolites. Moreover, since both Al and Ti behave as immobile elements during the bauxitization process [71], also the  $\text{TiO}_2/\text{Al}_2\text{O}_3$  ratio can be used as a reliable geochemical proxy of the nature of the source material [8]. The  $\text{TiO}_2/\text{Al}_2\text{O}_3$  values of the Abruzzi bauxites are very constant (ranging between 0.045 and 0.050, Figure 9f), both plotting in the nearby of the Upper Continental Crust values, as well as the other Mediterranean bauxites (with the notable exception of the Spinazzola, Gargano and Parnassos-Ghiona deposits). This represents another confirmation of the acid nature of the parent material that originated the Abruzzi bauxite ores.

## 7. Conclusions

The bauxite textures in the Abruzzi district range between oolitic and conglomeratic, likely pointing to erosion of older lateritic profiles, subsequent re-sedimentation on a karstic landscape, followed by reworking and diagenetic processes. Boehmite and hematite are the major minerals in the ooids, whereas kaolinite prevails in the matrix. Other minor constituents occur both as fine-grained detrital minerals (ilmenite, rutile, zircons, baddeleyite, monazite, xenotime) and as neo-formed phases (REE-fluoro-carbonates). The detection of authigenic REE-bearing minerals, together with the positive and negative Ce anomalies confirm that also in the case of the Abruzzi deposits, weathering and bauxite formation are effective processes for REE mobilization and enrichment in surficial environments. Further studies on this point are planned, in order to fully constrain the precise controls that different factors played in the REE redistribution. Scandium and Ga occur as trace elements in all the investigated bauxite profiles, and their distribution is chiefly controlled by the uptaking in neo-formed Fe- and Al-(hydr)oxides.

The new data obtained with the present study, integrated with the already published literature on other karst bauxites of the Mediterranean realm, suggest that the source materials of the Abruzzi bauxites were probably similar to those hypothesized (and partly proven) for the other bauxites of

the Apennine chain. These materials were possibly characterized by an acid nature, resulting from a combination of pyroclastic ashes and eolic dust, both originated from relatively distant sources.

**Author Contributions:** F.P., A.P.P. and N.M. carried out the fieldwork and the sampling activity. G.B., A.M. and A.P.P. collected the XRPD data. F.P., N.M. and M.B. performed the writing of the article and the data interpretation.

**Funding:** The research leading to these results has received funding by the “Programma per il finanziamento della ricerca di Ateneo 2016–Progetto CEB”, granted by Università degli Studi di Napoli Federico II (Italy) to Dr. Nicola Mondillo.

**Acknowledgments:** The first acknowledgement is due to the late Gy. Bárdossy, who long time ago introduced one of us (M. Boni) to the fascinating world of bauxite ores. We are also grateful to R. de’Gennaro for the help during SEM analyses. Thanks are due to three anonymous reviewers, whose comments were crucial in order to improve the earlier versions of our manuscript, and also to Q. Wang and G. Oggiano for editorial handling.

**Conflicts of Interest:** The authors declare no conflict of interest.

## References

1. Bárdossy, G.; Aleva, G.J.J. *Lateritic Bauxites*; Elsevier: Amsterdam, The Netherlands, 1990; 624p.
2. Ober, J.A. *Mineral Commodity Summaries, 2016*; US Geological Survey: Reston, VA, USA, 2016.
3. Ober, J.A. *Mineral Commodity Summaries, 2017*; US Geological Survey: Reston, VA, USA, 2017.
4. Herrington, R.; Mondillo, N.; Boni, M.; Thorne, R.; Tavlan, M. Bauxite and Nickel-Cobalt Lateritic Deposits of the Tethyan Belt. In *Tectonics and Metallogeny of the Tethyan Orogenic Belt*; Special Publication; Richards, J., Ed.; SEG Inc.: Littleton, CO, USA, 2016; Volume 19, pp. 349–387.
5. Bárdossy, G. *Karst Bauxites, Bauxite Deposits on Carbonate Rocks. Developments in Economic Geology 14*; Elsevier: Amsterdam, The Netherlands, 1982; 441p.
6. Boni, M. Bauxiti dell’Italia centrale, meridionale e della Sardegna (bibliografia ragionata). *L’Ind. Min.* **1972**, *1*, 1–32.
7. Bárdossy, G.; Boni, M.; Dall’Aglia, M.; D’Argenio, B.; Pantó, G. *Bauxites of Peninsular Italy: Composition, Origin and Geotectonic Significance*; Gebr. Borntraeger: Berlin, Germany, 1977; Volume 15, 61p.
8. Mondillo, N.; Boni, M.; Balassone, G.; Rollinson, G. Karst bauxites in the Campania Apennines (southern Italy): A new approach. *Periodico Mineralogia* **2011**, *80*, 407–432.
9. Boni, M.; Reddy, S.M.; Mondillo, N.; Balassone, G.; Taylor, R. A distant magmatic source for Cretaceous karst bauxites of southern Apennines (Italy) revealed through SHRIMP zircon age dating. *Terra Nova* **2012**, *24*, 326–332. [[CrossRef](#)]
10. Boni, M.; Rollinson, G.; Mondillo, N.; Balassone, G.; Santoro, L. Quantitative mineralogical characterization of karst bauxite deposits in the southern Apennines, Italy. *Econ. Geol.* **2013**, *108*, 813–833. [[CrossRef](#)]
11. Mongelli, G.; Boni, M.; Oggiano, G.; Mameli, P.; Sinisi, R.; Buccione, R.; Mondillo, N. Critical metals distribution in Tethyan karst bauxite: The Cretaceous Italian ores. *Ore Geol. Rev.* **2017**, *86*, 526–536. [[CrossRef](#)]
12. Chiochini, M.; Farinacci, A.; Mancinelli, A.; Molinari, V.; Potetti, M. Biostratigrafia a foraminiferi, dasicladali e calpionelle delle successioni carbonatiche mesozoiche dell’Appennino centrale (Italia). In *Biostratigrafia dell’Italia Centrale. Studi Geologici Camerti*; Mancinelli, A., Ed.; Università’ degli Studi di Camerino, Dipartimento di Scienze della Terra: Camerino, Italy, 1994; Volume Special, pp. 9–129.
13. Dewey, J.F.; Helman, M.L.; Turco, E.; Hutton, D.H.W.; Knott, S.D. Kinematics of the western Mediterranean. *J. Geol. Soc. Lond. Spec. Publ.* **1989**, *45*, 265–283. [[CrossRef](#)]
14. Malinverno, A.; Ryan, W.B. Extension in the Tyrrhenian Sea and shortening in the Apennines as a result of arc migration driven by sinking of the lithosphere. *Tectonics* **1986**, *5*, 227–246. [[CrossRef](#)]
15. Royden, L.; Patacca, E.; Scandone, P. Segmentation and configuration of subducted lithosphere in Italy: An important control on thrust-belt and foredeep-basin evolution. *Geology* **1987**, *15*, 714–717. [[CrossRef](#)]
16. Mazzoli, S.; Helman, M. Neogene patterns of relative plate motion for Africa-Europe: Some implications for recent Central Mediterranean tectonics. *Geol. Rundsch.* **1994**, *83*, 464–468.
17. Carmignani, L.; Oggiano, G.; Barca, S.; Conti, P.; Salvadori, I.; Eltrudis, A.; Funedda, A.; Pasci, S. Geologia della Sardegna (Note illustrative della Carta Geologica della Sardegna in scala 1: 200.000). *Mem. Descr. Carta Geol. d’Italia* **2001**, *60*, 1–283.

18. Vitale, S.; Amore, O.F.; Ciarcia, S.; Fedele, L.; Grifa, C.; Prinzi, E.P.; Tavani, S.; Tramparulo, F.D. Structural, stratigraphic, and petrological clues for a Cretaceous-Paleogene abortive rift in the Southern Adria domain (Southern Apennines, Italy). *Geol. J.* **2017**, *53*, 1–22. [[CrossRef](#)]
19. Parotto, M.; Praturlon, A. Geological summary of Central Apennines. *Quad. Ric. Sci.* **1975**, *90*, 257–311.
20. Scandone, P. Studi di geologia lucana: Carta dei terreni della serie calcareo-silico-marnosa e note illustrative. *Boll. Soc. Nat. Napoli* **1972**, *81*, 225–300.
21. D'Argenio, B.; Pescatore, T.; Scandone, P. Schema geologico dell'Appennino meridionale (Campania e Lucania). *Accad. Naz. Lincei* **1973**, *182*, 49–72.
22. Channell, J.E.T.; D'Argenio, B.; Horvath, F. Adria, the African promontory, in Mesozoic Mediterranean palaeogeography. *Earth Sci. Rev.* **1979**, *15*, 213–292. [[CrossRef](#)]
23. D'Argenio, B.; Mindszenty, A. Bauxites and related paleokarst: Tectonic and climatic event markers at regional unconformity. *Eclogae Geol. Helv.* **1995**, *88*, 453–499.
24. Carannante, G.; D'Argenio, B.; Ferreri, V.; Simone, L. Cretaceous paleokarst of the Campania Apennines: From the early diagenetic to late filling stage. A case history. *Rend. Soc. Geol. Ital.* **1987**, *9*, 251–256.
25. Carannante, G.; D'Argenio, B.; Mindszenty, A.; Ruberti, D.; Simone, L. Cretaceous-Miocene shallow water carbonate sequences. Regional unconformities and facies patterns. In Proceedings of the 15th IAS Regional Meeting, Ischia, Italy, 13–15 April 1994; pp. 27–60.
26. Mondillo, N.; Boni, M.; Balassone, G.; Piccolo Papa, A.; Putzolu, F.; Arfè, G. The Campo Felice and Monte Orsello bauxite occurrences (Abruzzi, Italy). In Proceedings of the 88th Congresso della Societa Geologica Italiana, Naples, Italy, 7–9 September 2016.
27. Putzolu, F.; Piccolo Papa, A.; Mondillo, N.; Boni, M.; Balassone, G.; Arfè, G. Bauxite in Abruzzi (Italy): The Campo Felice and Monte Orsello occurrences. *Appl. Earth Sci.* **2017**, *126*, 86–87. [[CrossRef](#)]
28. Eberli, G.P.; Bernoulli, D.; Sanders, D.; Vecsei, A. *From Aggradation to Progradation: The Maiella Platform, Abruzzi, Italy*; AAPG: Tulsa, OK, USA, 1993; Chapter 18.
29. D'Argenio, B.; Mindszenty, A.; Bárdossy, G.Y.; Juhasz, E.; Boni, M. Bauxites of southern Italy revisited. *Rend. Soc. Geol. Ital.* **1987**, *9*, 263–268.
30. Pouliot, G.; Hofmann, H.J. Florencite; a first occurrence in Canada. *Can. Mineral.* **1981**, *19*, 535–540.
31. Post, J.E.; Hughes, J.M. The crystal structure of parisite-(Ce),  $\text{Ce}_2\text{CaF}_2(\text{CO}_3)_3$ . *Am. Mineral.* **2000**, *85*, 251–258.
32. McDonough, W.F.; Sun, S.S. The composition of the Earth. *Chem. Geol.* **1995**, *120*, 223–253. [[CrossRef](#)]
33. Mongelli, G.; Boni, M.; Buccione, R.; Sinisi, R. Geochemistry of the Apulian karst bauxites (southern Italy): Chemical fractionation and parental affinities. *Ore Geol. Rev.* **2014**, *63*, 9–21. [[CrossRef](#)]
34. Laskou, M. Concentrations of rare earths in Greek bauxites. *Acta Geol. Hung.* **1991**, *34*, 395–404.
35. Deady, É.A.; Mouchos, E.; Goodenough, K.M.; Williamson, B.J.; Wall, F. A review of the potential for rare-earth element resources from European red muds: Examples from Seydişehir, Turkey and Parnassus-Giona, Greece. *Mineral. Mag.* **2016**, *80*, 43–61. [[CrossRef](#)]
36. Goodenough, K.M.; Schilling, J.; Jonsson, E.; Kalvig, P.; Charles, N.; Tuduri, J.; Deady, É.A.; Sadeghi, M.; Schiellerup, H.; Müller, A.; et al. Europe's rare earth element resource potential: An overview of REE metallogenetic provinces and their geodynamic setting. *Ore Geol. Rev.* **2016**, *72*, 838–856. [[CrossRef](#)]
37. Torró, L.; Proenza, J.A.; Aiglsperger, T.; Bover-Arnal, T.; Villanova-de-Benavent, C.; Rodríguez-García, D.; Ramírez, A.; Rodríguez, J.; Mosquea, L.A.; Salas, R. Geological, geochemical and mineralogical characteristics of REE-bearing Las Mercedes bauxite deposit, Dominican Republic. *Ore Geol. Rev.* **2017**, *89*, 114–131. [[CrossRef](#)]
38. Liu, X.; Wang, Q.; Zhang, Q.; Zhang, Y.; Li, Y. Genesis of REE minerals in the karstic bauxite in western Guangxi, China, and its constraints on the deposit formation conditions. *Ore Geol. Rev.* **2016**, *75*, 100–115. [[CrossRef](#)]
39. Proenza, J.A.; Aiglsperger, T.; Villanova-de-Benavent, C.; Torró, L.; Rodríguez-García, D.; Rodríguez, J. Discovery of REE minerals hosted in karst bauxite ores from the Sierra de Batoruco, Pedernales, Dominican Republic. In Proceedings of the 14th SGA Biennial Meeting, Quebec City, QC, Canada, 20–23 August 2017; Volume 4, pp. 1321–1324.
40. Trail, D. Redox-controlled dissolution of monazite in fluids and implications for phase stability in the lithosphere. *Am. Mineral.* **2018**, *103*, 453–461. [[CrossRef](#)]

41. Veilly, E.; Du Fou de Kerdaniel, E.; Roques, J.; Dacheux, N.; Clavier, N. Comparative behavior of britholites and monazite/brabantite solid solutions during leaching tests: A combined experimental and DFT approach. *Inorg. Chem.* **2008**, *47*, 10971–10979. [[CrossRef](#)] [[PubMed](#)]
42. Maksimovic, Z.; Pantó, G. Rare earth elements and nickel in the Grebnik diasporic bauxite deposit, Metohija (Kosovo). *Acta Geol. Hung.* **2004**, *47*, 259–268. [[CrossRef](#)]
43. Mongelli, G. Ce-anomalies in the textural components of Upper Cretaceous karst bauxites from the Apulian Carbonate Platform (southern Italy). *Chem. Geol.* **1997**, *140*, 69–79. [[CrossRef](#)]
44. Marni, P.; Mongelli, G.; Oggiano, G.; Dinelli, E. Geological, geochemical and mineralogical features of some bauxite deposits from Nurra (western Sardinia, Italy): Insights on conditions of formation and parental affinity. *Int. J. Earth Sci.* **2007**, *96*, 887–902. [[CrossRef](#)]
45. Kühnel, R.A. The role of cationic and anionic scavengers in laterites. *Chem. Geol.* **1987**, *60*, 31–40. [[CrossRef](#)]
46. Maksimovic, Z.; Panto, G.Y. Contribution to the geochemistry of the rare earth elements in the karst-bauxite deposits of Yugoslavia and Greece. *Geoderma* **1991**, *51*, 93–109. [[CrossRef](#)]
47. Vodyanitskii, Y.N. Geochemical fractionation of lanthanides in soils and rocks: A review of publications. *Eurasian Soil Sci.* **2012**, *45*, 56–67. [[CrossRef](#)]
48. Yang, L.; Wang, Q.; Zhang, Q.; Carranza, E.J.M.; Liu, H.; Liu, X.; Deng, J. Interaction between karst terrain and bauxites: Evidence from Quaternary orebody distribution in Guangxi, SW China. *Sci. Rep.* **2017**, *7*, 11842. [[CrossRef](#)] [[PubMed](#)]
49. Li, Z.; Din, J.; Xu, J.; Liao, C.; Yin, F.; Lu, T.; Cheng, L.; Li, J. Discovery of the REE minerals in the Wulong–Nanchuan bauxite deposits, Chongqing, China: Insights on conditions of formation and processes. *J. Geochem. Explor.* **2013**, *133*, 88–102. [[CrossRef](#)]
50. Derevyankin, V.A.; Porotnikova, T.P.; Kocherova, E.K.; Yumasheva, I.V.; Moiseev, V.E. Behavior of scandium and lanthanum in the production of alumina from bauxite (*in russian*). *Izv. Vyssh. Uchebn. Zaved. Tsvetn. Metall.* **1981**, 86–89.
51. Chassé, M.; Griffin, W.L.; O'Reilly, S.Y.; Calas, G. Scandium speciation in a world-class lateritic deposit. *Geochem. Perspect. Lett.* **2017**, *3*, 105–114. [[CrossRef](#)]
52. Vind, J.; Malfliet, A.; Bonomi, C.; Paiste, P.; Sajó, I.E.; Blanpain, B.; Tkaczyk, A.H.; Vassiliadou, V.; Pnias, D. Modes of occurrences of scandium in Greek bauxite and bauxite residue. *Miner. Eng.* **2018**, *123*, 35–48. [[CrossRef](#)]
53. Michard, A. Rare earth element systematics in hydrothermal fluids. *Geochim. Cosmochim. Acta* **1989**, *53*, 745–750. [[CrossRef](#)]
54. Kopeykin, V.A. Geochemical features of the behavior of gallium in laterization. *Geochem. Int.* **1984**, *21*, 16–20.
55. Losev, V.V. Gallium, indium, and thallium. In *Standard Potentials in Aqueous Solution*; CRC Press: Boca Raton, FL, USA, 1985; pp. 237–247.
56. Hieronymus, B.; Kotschoubey, B.; Boulègue, J. Gallium behaviour in some contrasting lateritic profiles from Cameroon and Brazil. *J. Geochem. Explor.* **2001**, *72*, 147–163. [[CrossRef](#)]
57. Mongelli, G.; Buccione, R.; Gueguen, E.; Langone, A.; Sinisi, R. Geochemistry of the Apulian allochthonous karst bauxite, Southern Italy: Distribution of critical elements and constraints on Late Cretaceous Peri-Tethyan palaeogeography. *Ore Geol. Rev.* **2016**, *77*, 246–259. [[CrossRef](#)]
58. Haniç, N. Geological and geochemical evolution of the Bolkardağı bauxite deposits, Karaman, Turkey: Transformation from shale to bauxite. *J. Geochem. Explor.* **2013**, *133*, 118–137. [[CrossRef](#)]
59. Karadağ, M.M.; Küpeli, Ş.; Arýk, F.; Ayhan, A.; Zedef, V.; Döylen, A. Rare earth element (REE) geochemistry and genetic implications of the Mortaş bauxite deposit (Seydişehir/Konya–Southern Turkey). *Chem. Erde* **2009**, *69*, 143–159. [[CrossRef](#)]
60. Laskou, M. Pyrite-rich bauxites from the Parnassos-Ghiona zone, Greece. In *Mineral Deposit Research: Meeting the Global Challenge*; Springer: Heidelberg, Germany, 2005; pp. 1007–1010.
61. Oggiano, G.; Marni, P. The bauxite of North-Western Sardinia. *Rend. Semin. Fac. Sci. Univ. Cagliari Suppl.* **2001**, *71*, 59–73.
62. Taylor, S.R.; McLennan, S.M. *The Continental Crust: Its Composition and Evolution*; Blackwell: Oxford, UK, 1985; pp. 1–312.
63. Rudnick, R.L.; Gao, S. Composition of the continental crust. *Treatise Geochem.* **2003**, *3*, 659.

64. Valetton, I.; Biermann, M.; Reche, R.; Rosenberg, F. Genesis of nickel laterites and bauxites in Greece during the Jurassic and Cretaceous, and their relation to ultrabasic parent rocks. *Ore Geol. Rev.* **1987**, *2*, 359–404. [[CrossRef](#)]
65. Dercourt, J.; Ricou, L.E.; Vrielynck, B. *Atlas Tethys Palaeoenvironmental Maps*; Gauthier-Villars: Paris, France, 1993; 307p.
66. Dercourt, J.; Gaetani, M.; Vrielynck, B.; Barrière, E.; Biju-Duval, B.; Brunet, M.F.; Cadet, J.P.; Crasquin, S.; Sandulescu, M.E. *Atlas Peri-Tethys, Palaeogeographical Maps*; CCGM/CGMW: Paris, France, 2000; 269p.
67. Patacca, E.; Scandone, P. Geology of the southern Apennines. *Boll. Soc. Geol. Ital.* **2007**, *7*, 75–119.
68. Comer, J.B. Genesis of Jamaican bauxite. *Econ. Geol.* **1974**, *69*, 1251–1264. [[CrossRef](#)]
69. Cuadros, J.; Diaz-Hernandez, J.L.; Sanchez-Navas, A.; Garcia-Casco, A. Role of clay minerals in the formation of atmospheric aggregates of Saharan dust. *Atmos. Environ.* **2015**, *120*, 160–172. [[CrossRef](#)]
70. Kalaitzidis, S.; Siavalas, G.; Skarpelis, N.; Araujo, C.V.; Christanis, K. Late Cretaceous coal overlying karstic bauxite deposits in the Parnassus-Ghiona Unit, Central Greece: Coal characteristics and depositional environment. *Int. J. Coal Geol.* **2010**, *81*, 211–226. [[CrossRef](#)]
71. MacLean, W.H.; Bonavia, F.F.; Sanna, G. Argillite debris converted to bauxite during karst weathering: Evidence from immobile element geochemistry at the Olmedo Deposit, Sardinia. *Miner. Depos.* **1997**, *32*, 607–616. [[CrossRef](#)]



© 2018 by the authors. Licensee MDPI, Basel, Switzerland. This article is an open access article distributed under the terms and conditions of the Creative Commons Attribution (CC BY) license (<http://creativecommons.org/licenses/by/4.0/>).